Erman, C., Yolsal-Çevikbilen, S., Eken, T., Tilmann, F., Keleş, D., Taymaz, T. (2022): Constraints on the Lithospheric Kinematics in the Aegean and Western Anatolia Unveiled by SKS Splitting Observations. - Journal of Geophysical Research: Solid Earth, 127, 12, e2022JB025265.

https://doi.org/10.1029/2022JB025265

JGR Solid Earth

RESEARCH ARTICLE
10.1029/2022JB025265

Constraints on the Lithospheric Kinematics in the Aegean and Western Anatolia Unveiled by SKS Splitting Observations

C. Erman[1], S. Yolsal-Çevikbilen[1], T. Eken[1], F. Tilmann[2,3], D. Keleş[1], and T. Taymaz[1]

[1]Department of Geophysical Engineering, The Faculty of Mines, Istanbul Technical University, Istanbul, Turkey, [2]Department of Geophysics, Deutsches GeoForschungsZentrum GFZ, Potsdam, Germany, [3]Department of Earth Sciences, Institute of Geological Sciences, Freie Universitat, Berlin, Germany

Key Points:

- Observed seismic anisotropy can be explained by a combined effect of internal deformation of the mantle lithosphere and asthenosphere
- The presence of two-layer anisotropy is obtained beneath the upper mantle of NW Anatolia
- A distinct counter-clockwise rotation of average fast polarization directions from north to south of the Aegean region is estimated

Supporting Information:

Supporting Information may be found in the online version of this article.

Correspondence to:

C. Erman,
ermanc@itu.edu.tr

Citation:

Erman, C., Yolsal-Çevikbilen, S., Eken, T., Tilmann, F., Keleş, D., & Taymaz, T. (2022). Constraints on the lithospheric kinematics in the Aegean and western Anatolia unveiled by SKS splitting observations. *Journal of Geophysical Research: Solid Earth*, *127*, e2022JB025265. https://doi.org/10.1029/2022JB025265

Received 26 JUL 2022
Accepted 25 NOV 2022

Author Contributions:

Conceptualization: C. Erman, S. Yolsal-Çevikbilen, T. Eken, F. Tilmann, T. Taymaz
Data curation: C. Erman, S. Yolsal-Çevikbilen, T. Eken, D. Keleş
Formal analysis: C. Erman, S. Yolsal-Çevikbilen, T. Eken, F. Tilmann, D. Keleş, T. Taymaz
Investigation: C. Erman, S. Yolsal-Çevikbilen, T. Eken, F. Tilmann, T. Taymaz
Methodology: C. Erman, S. Yolsal-Çevikbilen, T. Eken, F. Tilmann, D. Keleş
Project Administration: C. Erman, S. Yolsal-Çevikbilen
Resources: C. Erman
Software: C. Erman, T. Eken, F. Tilmann
Supervision: C. Erman, S. Yolsal-Çevikbilen, T. Taymaz

Abstract The present study investigates azimuthal anisotropy and its relation to the geodynamical processes beneath the back-arc of the Hellenic subduction zone in the eastern Aegean and western Anatolia where surface tectonics is dominated by the right-lateral strike-slip North Anatolian Fault Zone (NAFZ) in the north and E-W oriented normal fault systems. We obtained apparent SKS splitting parameters from 1,660 good quality and 137 null measurements extracted from 542 events recorded at 40 permanent broadband seismic stations. Overall, the station-averaged splitting parameters indicate NNE-SSW oriented fast directions (~N20°E) and splitting delays around ~1.5 s. The large splitting delays, particularly observed beneath the northern Aegean can be explained by either an enlarged mantle wedge thickness or increased strength of upper mantle anisotropy. We constrain complex anisotropy structures within two layer models from notable backazimuthal variations in individual splitting measurements observed beneath a few stations at the north located in a close proximity to the NAFZ and central-western Anatolia. At the western end of the NAFZ, our estimated upper layer anisotropy direction (at ~120 km) is rather parallel to the NAFZ reflecting the imprint of a lithospheric petrofabric formed by recent deformation while in central-western Anatolia they correlate well with maximum shear directions and small splitting delays (~0.6 s) appear to further support relatively thin lithosphere (~90 km). An overall pattern of extension-parallel fast directions (N10°E) within lower layer can be attributed to the slab rollback-induced mantle flow that is highly oblique with respect to the WSW-ward motion of the Anatolian lithosphere.

Plain Language Summary Seismological constrains on uppermost mantle structures provide essential information for better understanding of the geodynamic processes that have shaped the current deformation in complex tectonic regions. To investigate the seismic anisotropy, which is the directional dependence of seismic wave velocities, and its relation to the geodynamical processes in the upper mantle of eastern Aegean and western Anatolia, we performed splitting measurements on core-mantle refracted shear waves recorded by 40 permanent broadband seismic stations. We overall estimate NE-SW oriented fast polarization directions, and delay times between 0.65 and 2.2 s. The results imply that the origin of observed seismic anisotropy can be mostly explained by a combined effect of an internal deformation of the mantle lithosphere and asthenosphere. Our findings reveal the presence of two-layer anisotropy outlining complicated structures, primarily in the upper mantle of NW Anatolia associated with the western end of North Anatolian Fault Zone. Future numerical modeling and anisotropy studies should be considered to test these results for further interpretation.

1. Introduction

The relative convergent movement between the Eurasian, African, and Arabian plates has exerted a major influence on the tectonic evolution of Anatolia and surrounding regions (Figures 1a and 1b). It is also responsible for the W-SW directed escape motion of the Anatolian plate (e.g., McKenzie, 1972; Taymaz, 1996) and resultant seismotectonic structures. Intense earthquake activity is particularly localized along the Hellenic subduction zone, western Anatolia, the right-lateral North Anatolian Fault Zone (NAFZ) and the left-lateral East Anatolian Fault Zone (EAFZ). The geodynamic evolution of the region is shaped by the closure of the Tethys Ocean. This event had a significant influence on shaping the active tectonics of Anatolia and surroundings. The 1,500 km long NAFZ, the northern boundary of the Anatolian Plate, starts from the Karlıova triple junction in the east, and reaches to the western edge of the Aegean block by passing through the North Aegean Trough (NAT) (McKenzie, 1972, 1978; Taymaz et al., 1990, 1991). Geodetic (GPS) measurements (e.g., McClusky et al., 2000, 2003; Nocquet, 2012; Reilinger et al., 2006) indicated average slip rates of about 25 mm/yr and

Validation: C. Erman, S. Yolsal-Çevikbilen, T. Eken, F. Tilmann, T. Taymaz
Visualization: C. Erman
Writing – original draft: C. Erman, S. Yolsal-Çevikbilen, T. Eken, F. Tilmann, D. Keleş, T. Taymaz
Writing – review & editing: C. Erman, S. Yolsal-Çevikbilen, T. Eken, F. Tilmann, D. Keleş, T. Taymaz

10 mm/yr along the NAFZ and EAFZ, respectively. The Hellenic Trench retreated ~580 km since the Miocene (Brun & Faccenna, 2008; Jolivet & Faccenna, 2000; McKenzie, 1972), leading to a N-S and NE-SW directed extensional tectonic regime in the Aegean and western Anatolia. Pulling and pushing forces exerted as the consequence of the Hellenic subduction zone in the west and collision process between Arabian and Anatolian plates in the east induce the SW-directed movement of Anatolia and presumably control the lithospheric thickness variation throughout Anatolia (e.g., Le Pichon & Angelier, 1979; McKenzie, 2020; Meijer & Wortel, 1997; Taymaz et al., 2007). For instance, the relative NW-directed movement of the Arabian plate with respect to Eurasia with an average velocity of 18 mm/yr results in crustal shortening and thickening in eastern Anatolia. However, the retreat of the Hellenic trench induces extensional forces causing crustal thinning and stretching in the Aegean and western Anatolia (Jolivet et al., 2009, 2013, 2018; Sodoudi et al., 2006). Nocquet (2012) further reported that horizontal strain rates increased toward the Hellenic trench (Figure 1c).

Since the fast axis of olivine minerals aligns with maximum finite strain under high strain conditions, due to so-called lattice preferred orientation (LPO), seismic anisotropy can be used to constrain current mantle flow and fossil fabrics (e.g., Fouch & Rondenay, 2006; Karato, 1987; Zhang & Karato, 1995). Usually, a hexagonal symmetry is assumed for the petrofabric arising from the partial alignment of olivine. Splitting of SKS waves has emerged as a widely used method for characterizing vertically integrated azimuthal anisotropy (Savage, 1999; Silver & Chan, 1991). It is characterized by the two splitting parameters: the fast polarization direction (FPD), representing the azimuth of the fast anisotropic symmetry axis, and the splitting delay time (DT), which is related to the strength of anisotropy and the thickness of the anisotropic layer (Silver & Chan, 1991). It is therefore sensitive mostly to mantle flow with horizontally oriented shearing directions, for example, the movement of lithospheric plates with respect to the deeper mantle. In particular, regions of vertical flow generally show up as regions of absent splitting or small DTs. In most tectonic environments, detected seismic anisotropy is primarily linked to the aligned mineral orientation in the upper mantle below the stations, as typically measured DTs larger than ~1 s can generally not be explained solely by crustal anisotropy and because the organized mineral alignment only occurs when deformation involves dislocation creep, which is usually the case only at upper mantle depths (e.g., Karato & Wu, 1993; Savage, 1999).

The main focus of this study is to investigate the upper mantle anisotropy beneath 40 broadband seismic stations (Figure 2a and Table S1 in Supporting Information S1) located at Skyros, Lesvos and Samothraki Islands, North Aegean Sea, Biga Peninsula (NW Anatolia), North Aegean Sea and Gulf of Gökova. To achieve this, we performed shear wave (SKS) splitting analysis, initially assuming single-layer anisotropic structure with a horizontally oriented symmetry axis. Lateral variations of our station-averaged splitting parameters appear to be consistent with previous findings in the same region and for those stations with previous measurements and therefore favor a regional sub-lithospheric origin of anisotropy for the entire study area. For several permanent stations with long time-period operations we noted azimuthal dependencies of inferred splitting parameters, which can only be explained with more complex anisotropic structures. Specifically, the observations for these stations can be explained with two layer anisotropic structures, where the upper layer corresponds to strain in the lithosphere and the lower layer indicates asthenospheric mantle flow induced by slab rollback.

2. Previous Studies

2.1. On Anisotropy

Most works on seismic anisotropy in Anatolia and the Aegean primarily rely on SWS measurements (e.g., Biryol et al., 2010; Confal et al., 2016; Evangelidis, 2017; Evangelidis et al., 2011; Haztfeld et al., 2001; Kaviris et al., 2018; Lemnifi et al., 2017; Merry et al., 2021; Olive et al., 2014; Paul et al., 2014; Sandvol et al., 2003; Schmid et al., 2004;Yolsal-Çevikbilen, 2014; Figure 1c).

Practically all studies find a pervasive pattern of broadly NE-SW FPDs for the entire region, which is generally attributed to an instantaneous density-driven mantle flow in the asthenosphere. The FPDs only deviate from the dominant NE-SW pattern toward southwestern Anatolia and the Peloponnese exhibiting a more complex pattern, possibly due to the suspected slab tearing (Paul et al., 2014) and return flow (Evangelidis et al., 2011; Olive et al., 2014). In the back-arc area of the Aegean, a gradual increase in DTs observed from south to north, is attributed to the NE-SW directed mantle wedge flow that is induced by the retreating African slab (Evangelidis et al., 2011; Hatzfeld et al., 2001; Paul et al., 2014).

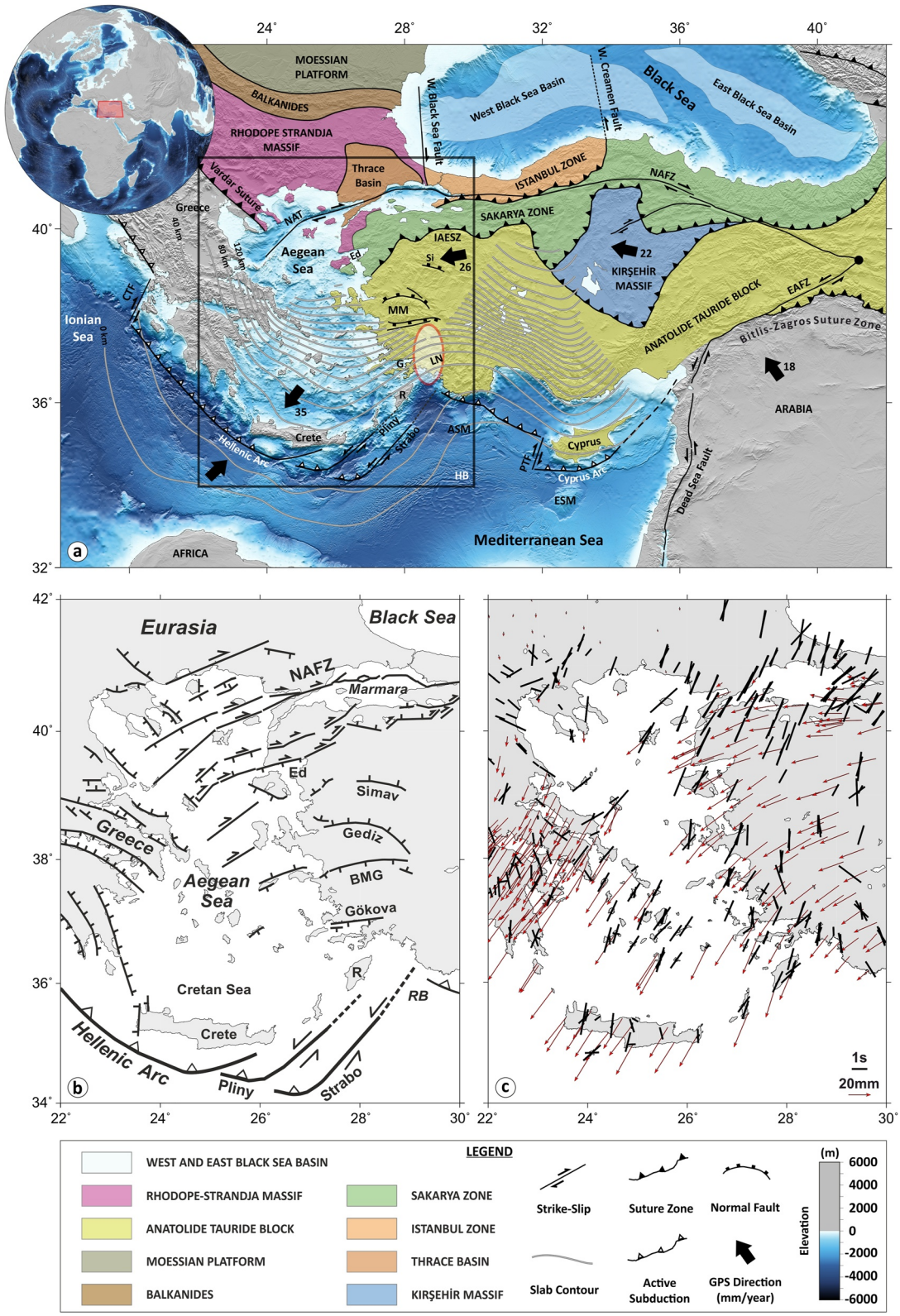

Figure 1.

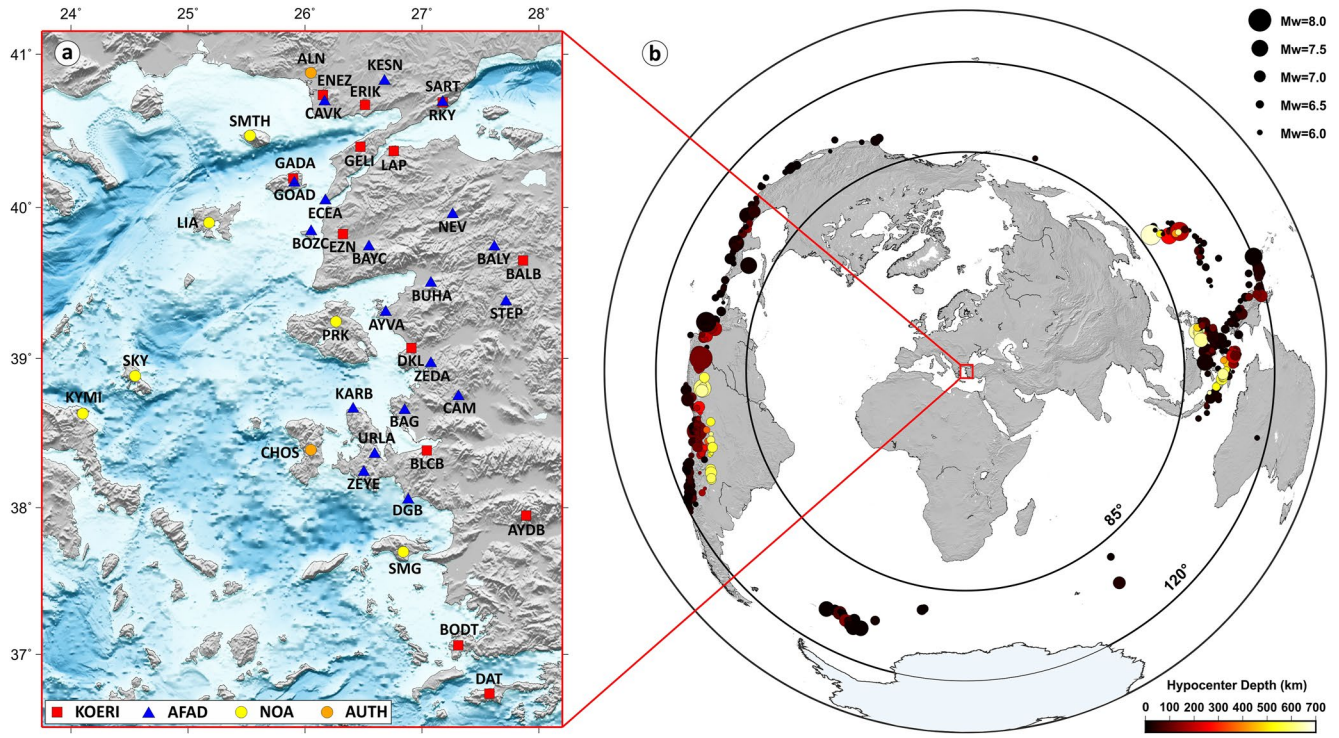

Figure 2. (a) Locations of 40 broadband seismic stations analyzed in this study. (b) Spatial distribution of 542 teleseismic events (colored circles) which yielded good splitting measurements (see Table S2 for details). The size of the circles and filling colors are proportional to the magnitude and focal depth of the events, respectively. The study area is marked with red box. Circles indicate epicentral distances of 85° and 120°.

At the eastern side of the Hellenic subduction zone, based on source-side anisotropy measurements focusing on the sub-slab region, Evangelidis (2017) observed a general trench-normal pattern that was likely associated with mantle flow developing in response to a possible ongoing tearing of the oceanic lithosphere. According to Evangelidis (2017), trench-parallel SKS measurements would imply a tear that has not yet reached the surface. Confal et al. (2018) tested with a petrological-thermo-mechanical model various factors that have likely influenced the *N-S* asthenospheric mantle flow, that is, the slab rollback along with Nubian-Eurasian plate convergence in the Aegean Sea, a slab tear in the African subducting plate, and the slab break-off of the Arabian plate. Their model predicts similar regional coherency as observed, with predicted DTs of up to 2 s.

Despite the apparent consistency for the lateral variations of SKS splitting measurements, some other observations for instance, a systematic increase for splitting DTs to the north of the Aegean as noted by Hatzfeld et al. (2001) was explained by the joint contribution of the mantle lithosphere and some part of the asthenosphere on the observed anisotropic signal. Similarly, Paul et al. (2014) suggested a thicker mantle wedge in the northern part can be the reason for relatively strong anisotropy. Endrun et al. (2011) were the first to infer a vertically stratified seismic anisotropy model based on the inversion of surface waves (e.g., Rayleigh waves) but for a limited part that only covered Aegean Sea. More recently, horizontal slices extracted from 3-D anisotropic *P*-wave traveltime

Figure 1. (a) A schematic map of the Eastern Mediterranean with the main suture zones, tectonic structures, and boundaries compiled from Taymaz et al. (1990, 1991, 2004, 2007, 2022), Okay and Tüysüz (1999), Okay (2008), Yolsal-Çevikbilen and Taymaz (2012) and Yolsal-Çevikbilen et al. (2012). Black arrows exhibit relative plate motions with respect to Eurasia (McClusky et al., 2000, 2003; Nocquet, 2012; Reilinger et al., 2006). The rectangular box outlines the study area shown in (b) Gray lines represent the slab contours of Hellenic and Cyprus subduction zones with 20 km interval (see Hayes et al., 2018). Bathymetry and topography data are taken from GEBCO (2019) and SRTM15+V2 (Tozer et al., 2019), respectively. Red ellipsoid at SW Turkey shows the location of the slab tear on subducted African lithosphere (Biryol et al., 2011; Confal et al., 2020). (b) A generic tectonic map of the Aegean region and western Anatolia with major geological structures (Mascle & Martin, 1990; Şaroğlu et al., 1992; Taymaz et al., 1990, 1991, 2004, 2022; Yolsal-Çevikbilen et al., 2014). (c) Map of the average splitting parameters (black bars) reported by Vinnik et al. (1992), Hatzfeld et al. (2001), Schmid et al. (2004), Evangilidis et al. (2011), Paul et al. (2014), Olive et al. (2014), Confal et al. (2016), Evangelidis (2017), and Kaviris et al. (2018). GPS vectors (red arrows) are shown relative to stable Eurasia, as reported by Nocquet (2012). Abbreviations: ASM: Anaximander Sea Mountains, CTF: Cephalonia Transform Fault, EAFZ: East Anatolian Fault Zone, Ed: Gulf of Edremit, ESM: Eratosthenes Sea Mountains, G: Gulf of Gökova, HB: Herodotus Basin, IAESZ: İzmir-Ankara-Erzincan Suture Zone, LN: Lycian Nappes, MM: Menderes Massif, NAFZ: North Anatolian Fault Zone, NAT: North Aegean Trough, PTF: Paphos Transform Fault, R: Rhodes Island, Si: Simav Graben.

tomography images at the depths of 100 and 150 km beneath the Eastern Mediterranean and Middle East by Wei et al. (2019) confirmed NE-SW-oriented fast directions in most of Anatolia, a circular flow around the tear in southwestern Anatolia, and anisotropic orientations parallel to the trench in the fore-arc and sub-slab regions. Earlier Wei et al. (2019) computed synthetic path-integrated single layer SKS splitting parameters by using their anisotropic *P*-wave velocity model. A strong consistency between previously observed SKS splitting and those synthetic SKS splitting estimates validated the reliability of their vertically stratified anisotropic model with *P*-wave fast directions.

In mainland Turkey, anisotropic inversions of Pn waves characterizing the shallowest mantle (Al-Lazki et al., 2003, 2004; Kömeç-Mutlu & Karabulut, 2011) and SKS-derived anisotropic orientations in the lithosphere (e.g., Paul et al., 2014; Sandvol et al., 2003) show consistent fast directions, suggesting vertically coherent deformation in the mantle lithosphere. Vertically coherent deformation throughout the whole lithosphere has finally been demonstrated by the most recent anisotropic *P*-wave tomography work of Wang et al. (2020), who observed fast directions in the lower crust and uppermost mantle parallel to the regional maximum extensional directions in western Turkey.

2.2. Lithospheric Structure and Deformation

Kinematic models derived from seismicity and geodetic data imply that western Anatolia and Aegean region are the most actively deforming parts of the Anatolian plate (Kreemer et al., 2004; Le Pichon & Kreemer, 2010; Reilinger et al., 2006). Regional tectonics and seismicity are primarily controlled by different scale normal and strike-slip faults especially located in the Aegean Sea and surroundings. Particular, E-W oriented horst and grabens (i.e., Edremit, Gediz, Simav, Büyük Menderes, Küçük Menderes, Gökova) are developed associated to the active faults in western Turkey. Barka and Reilinger (1997) observed a west-to-east decrease in extension rates along the grabens. Focal mechanisms of earthquakes also imply normal faulting with right-lateral strike-slip components (Saltogianni et al., 2015; Taymaz et al., 1991; Yolsal-Çevikbilen et al., 2014).

Early observations and models inferred from geophysical and seismological approaches (e.g., gravity measurements, receiver function and seismic tomography) exhibit both E-W and N-S varying nature of crustal and lithospheric thickness along the study region (e.g., Biryol et al., 2011; Confal et al., 2020; Çubuk-Sabuncu et al., 2017; Fichtner, Saygin, et al., 2013, Fichtner, Trampert, et al., 2013; Karabulut et al., 2013; Kind et al., 2015; Saunders et al., 1998; Salaün et al., 2012; Sodoudi et al., 2006; Tirel et al., 2004; Vanacore et al., 2013). Various receiver function analysis techniques including H-k stacking, direct 1-D inversion, or stacked images of depth migrated receiver functions in several early studies (e.g., Karabulut et al., 2013; Saunders et al., 1998; Sodoudi et al., 2006; Vanacore et al., 2013) provide common evidences for the thin crust beneath the Aegean and western Anatolia. In Aegean Sea, 20–22 km of crustal thicknesses at the southern Aegean, somewhat thick crust (∼25–28 km) at the northern Aegean Sea and ∼26–30 km relatively thick crust at Cyclades were earlier reported (Kind et al., 2015; Sodoudi et al., 2006; Tirel et al., 2004). Crustal thickness in western Anatolia is about 30 km, but to the north, relatively thick crust with about 40 km had been measured at the southwest coast of the Marmara Sea (e.g., Delph et al., 2015; Vanacore et al., 2013). The mantle lithosphere is thickening toward the north, particularly underneath the Istanbul and Pontides block, north of the NAFZ with a prominent high *P*-wave speeds (at depth <150 km), revealed in the most recent high-resolution teleseismic tomography images (e.g., Confal et al., 2020; Wei et al., 2019), can be associated to the Neotethyan sutures (Okay & Tüysüz, 1999).

3. Data and Methods

3.1. Data

In this study, we used waveforms of SKS arrivals recorded at 40 broadband seismic stations (Table S1 in Supporting Information S1; Figure 2a) operated by FDSN networks KO (Kandilli Observatory and Earthquake Research Institute, Boğaziçi University, 1971), TU (Disaster and Emergency Management Authority, 1990), HL (National Observatory of Athens, Institute of Geodynamics, 1975) and HT (Aristotle University of Thessaloniki Seismological Network, 1981). The data were retrieved via the Incorporated Research Institute for Seismology (IRIS-DMC; https://ds.iris.edu/wilber3/find_event), European Integrated Data Archive (EIDA; http://eida.koeri.boun.edu.tr/webinterface) and Earthquake Data Centre System of Turkey (AFAD-DDA; http://tdvm.afad.gov.tr/). Figure 2b presents the global distribution of teleseismic earthquakes used, with eastern (Indonesia, Papua New Guinea) and

southwestern to northwestern back azimuths (western margins of South and Central America), with an isolated cluster related to the South Sandwich subduction zone in the SSW.

3.2. Methods: SKS Splitting Analyses

SKS splitting measurements for individual station-event pairs were performed using two different techniques: Eigenvalue (EV) and Transverse Energy Minimization (TE), following Silver and Chan (1991). We define an analysis window of 60 s (30 s before and after the SKS phase onset), taking care to include solely SKS phases to avoid contamination by other seismic phases, that is, S, ScS, SS or sS, based on IASPI91 theoretical arrival times (Kennett & Engdahl, 1991). In this way we obtained 19,239 two-component waveforms extracted from 2,719 teleseismic events. Finally, a total of 542 earthquakes occurred within an epicentral distances range from 85° to 120°, and with magnitudes (M_w) larger than 5.5 between 2004 and 2021 were analyzed (Table S2).

For individual SKS splitting measurements, we initially used the "*Automated Shear Wave Splitting*" algorithm (Teanby et al., 2004) that is based on the EV method of Silver and Chan (1991). The details of this method are given in Supporting Information S1. Besides as an alternative approach we applied the TE approach (Silver & Chan, 1991) that is implemented in the "*multisplit*" software (Eken & Tilmann, 2014). We used a fixed window length (40 s) including 15 s before and 25 s after the SKS phase onset. To better isolate SKS phase signal with improved SNR, we applied a band-pass filter between 0.05 and 0.25 Hz, the same range as used for most of the EV-based splitting measurements. Later, station-averaged splitting parameters were calculated using the misfit surface stacking (Wolfe & Silver, 1998) and Von Mises approach (Cochran et al., 2003). The observed discrepancies between the mean splitting parameters obtained from the two different averaging techniques will be further discussed in the following sections. Eken et al. (2013) suggested that the misfit surface stacking approach could, in general, give more reliable results under the presence of single-layer simple anisotropy with horizontal symmetry axis. In cases of two-layer anisotropy structure, which becomes evident by systematic backazimuthal variation of apparent splitting parameters, none of the averaging technique of individual anisotropic parameters measured under single horizontal anisotropic layer will be appropriate and an identification of seismic anisotropy will require the estimation of two-layer anisotropy parameters.

Quantifying uncertainties of individual splitting measurements is essential in order to make an assessment of their reliability and thus to avoid misinterpretation between genuine splitting results and null measurements. To achieve this, we employ the inverse *F*-test error analysis following Silver and Chan (1991). This test provides a statistical measure of the significance of any increase from the minimum of the misfit surface according to the preset confidence level, usually set to 95%. The inverse *F*-test analysis highly depends on the number of degrees of freedom in the data and parameters. We set this one to per second for each component according to Silver and Chan (1991) suggesting it as a good value in the case of teleseismic events.

3.3. Two-Layer Anisotropy Investigations

Based on a notable azimuthal variation of apparent SKS splitting parameters detected for a few permanent stations (e.g., GELI, LAP, RKY) with long-term operation, we investigate potential two-layer anisotropy beneath these seismic stations. A proper model resolution for the four splitting parameters within a two-layered anisotropic structure (FPD_{upper}, DT_{upper} and FPD_{lower}, DT_{lower}) requires a high-quality data set with good azimuthal coverage. We utilized again the "multisplit" software (Eken & Tilmann, 2014) in which optimal two-layer splitting parameters and their uncertainties are estimated through a grid search over a range of splitting parameters for each layer following the approach of Silver and Savage (1994). The resultant error "surface" (really a 4D space) represents the calculated residual transverse energy values obtained after performing the inverse two-layer splitting operator with a range of DT and FPD pairs for upper and lower layers over each individual event at the station of interest. In the two-layer grid search, we varied the DTs in steps of 0.05 s (from 0 to 3 s) and the FPDs in steps of 5° (from 0° to 180°) in each layer. Final model parameters were estimated by stacking error surfaces as described in Wolfe and Silver (1998). In order to test the variability of two-layer splitting parameters, in the next stage, we performed 250 realizations by bootstrap resampling the event error surfaces prior to stacking. The distribution of the bootstrap estimates gives an idea about the variance of final model parameters. We further applied a jackknife test to have an insight into the stability of two-layer grid search results. To do this, we performed the same approach described above 200 times on randomly generated sub-data sets, which included 70% of the actual data set. The

variance of all parameters derived from the 200 random realizations provides an insight into the robustness of the final two-layer anisotropic model beneath the station of interest.

For the stations with a small number of SKS observations and lack of good azimuthal data coverage (e.g., DGB, URLA, and ZEYE) the grid search approach did not result in well-constrained two-layer models. For these stations, we further performed a curve fitting approach that helped to reach optimum two-layer anisotropic models. To achieve this, we applied the "M-Split" software that is a MATLAB-based utility originally developed by Abgarmi and Arda Özacar (2017). It estimates optimum two-layer models with associated standard deviations. During this search, we let upper and lower layer FPDs vary between 0° and 180° with a step of 1°. The upper layer DTs is varied between 0.1 and 2.0 s with 0.1 s increments while for the lower layer DTs range between 0.5 and 2.0 s with a step of 0.1 s considering the DT values beneath the sub-lithospheric layer of the study area obtained by this and previous studies mentioned above. In order to assess how efficiently a two-layer model fits the observations compared to a single-layer model, we consider the R^* values (Walker et al., 2005) that were derived for the obtained best-fit two-layer models. This value is dependent on the number of splitting measurements, number of model parameters and standard misfit reduction value and range from $-\infty$ to 1. For example, $R^* > 0.25$ means that the two-layer models explain more than 25% of the azimuthal variation of the splitting parameters (Fontaine et al., 2007; Walker et al., 2005). We employ a minimum threshold of R^* of 0.45 in order to favor a two-layer anisotropic model over a single-layer one.

4. Results

A careful evaluation procedure including a visual inspection was performed over the 19,239 SKS-phase signals, finally yielding 1,860 and 1,660 good non-null splitting estimates based on the EV and TE methods, respectively. 137 out of all good null-splitting measurements were confirmed by both methods.

4.1. Non-Null Splitting Measurements

Figures 3a and 3b show good non-null and null splitting examples obtained from TE method, respectively. We divide the seismic stations into 4 main groups by considering their locations in different tectonic units (Figure 4a). Group A stations are in the Thrace Basin (TB), group B stations in the Rhodope-Strandja Massif, group C stations are located in the Sakarya Zone (SZ), and group D stations in the Anatolide-Tauride Block. Station GOAD, which is located at the boundary of group B, was not considered for further interpretations because an insufficient number of splitting measurements for this station (only 3). Similarly, stations SKY and KYMI located in mainland Greece, western Aegean, far from the other stations in any group, were not included the group averages. The spatial distribution of average FPDs and DTs is presented in Figure 4b. Table 1 presents a summary of average splitting parameters with their relevant uncertainties.

We here describe splitting results obtained from the TE method (Silver & Chan, 1991). Figure 4c shows directional variation of all individual apparent splitting parameters estimated for the different groups. For groups A, B, C the splitting estimates indicate NE-SW FPDs for most azimuths and backazimuthal variation of splitting parameter is very similar, with a linear trend of apparent FPDs for backazimuths 240°–300°. For group D stations, FPDs over most azimuths are close to N10E direction, except for backazimuths 270°–360°, for which a few measurements indicate NNW-SSE directions, while others in the same range show NNE-SSW FPDs as observed for the rest of the backazimuthal range.

We estimated station-averaged splitting parameters based on the stacked misfit surface (Wolfe & Silver, 1998), with a maximum of 95 (station RKY) and minimum of 3 individual SKS measurements (station GOAD). The average of all splitting indicates a FPD oriented along N21°E ± 10° and DT of 1.55 s ± 0.33, where the ranges represent the standard deviation of individual measurements. The average FPDs and DTs calculated for each station vary between N2°W to N46°E and 0.65–2.2s, respectively (Table 1; Figures S1 and S2 in Supporting Information S1). Station-averaged FPDs calculated for group A in the TB, group B in the RSM, and group C in the SZ are very similar (e.g., found as ~N23°E ± 3°, N25°E ± 4°, and N23°E ± 3°, respectively) (Figure 4b). However, group *D* in the Anatolide Tauride Block (ATB) is represented by a station-averaged FPDs averaging ~N8°E ± 4° direction indicating a significant counter-clockwise rotation at the south of the SZ. Station-averaged DTs were calculated as 1.74 ± 0.14 s, 1.68 ± 0.16 s, and 1.68 ± 0.15 s for group A, B, and C, respectively. Splitting DTs for stations in group *D* are smaller with a station average of 1.33 ± 0.15 s (Figure 4b). These

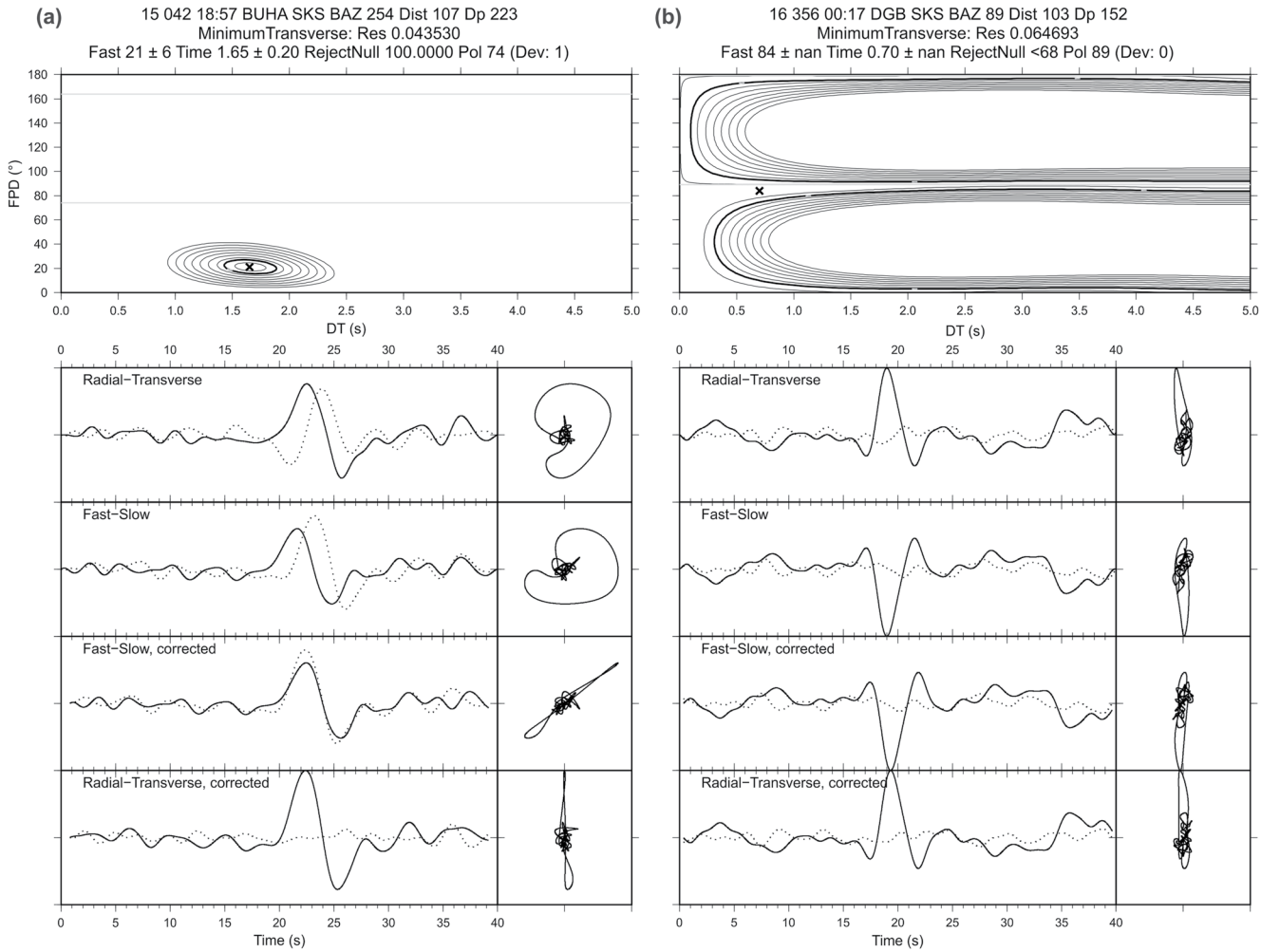

Figure 3. Examples of good non-null SKS splitting (a) and null (b) analysis following the tangential energy minimization method for the same event-station pair as shown in Figure 4. Misfit surface with well-defined splitting parameters is shown at top, with thick contour indicating 95% confidence region. Radial (solid line)—Transverse (dotted line) and Fast (dotted line)—Slow (solid line) components are shown below, with their particle motions before and after splitting correction.

observations confirm spatial coherency between the stations located in northern geological units as TB, RSM and SZ whereas mean FPD for the stations in ATB unit is more at the NNE-SSW direction compared to the northern stations (Figure 5). We compared these results with the Von Mises Averaging approach (Cochran et al., 2003) in Figure S3 in Supporting Information S1 and observed that averages from both methods were broadly consistent. There is also a good accordance between station averaged results obtained from EV method (please see Supporting Information S1) and from TE method (Table 1 and Figure S4 in Supporting Information S1). Noticeable differences were only detected between station-averaged FPDs at station AYDB and SMTH with discrepancies of ∼24° and ∼30°, respectively (Table 1 and Figure S4 in Supporting Information S1). To investigate whether such large angular misfits stem from the possible sensor misorientation of both stations, we conducted a simple *P*-wave polarization method described in Niu and Li (2011). We calculated 5.2° ± 3.7 and 7.6° ± 4.0 of sensor misorientations for stations SMTH and AYDB as these do not appear to be large enough to cause significant differences between the FPDs derived from EV and TE methods. Similarly, Büyükakpınar et al. (2021) estimated relatively insignificant sensor misorientation (as 7.6° ± 1.3) at the station AYDB as 7.6° ± 1.3 through *P*-wave polarization analysis performed on 84 events. The details of the method used for polarization analysis are given in Supporting Information S1 (Figure S5 in Supporting Information S1).

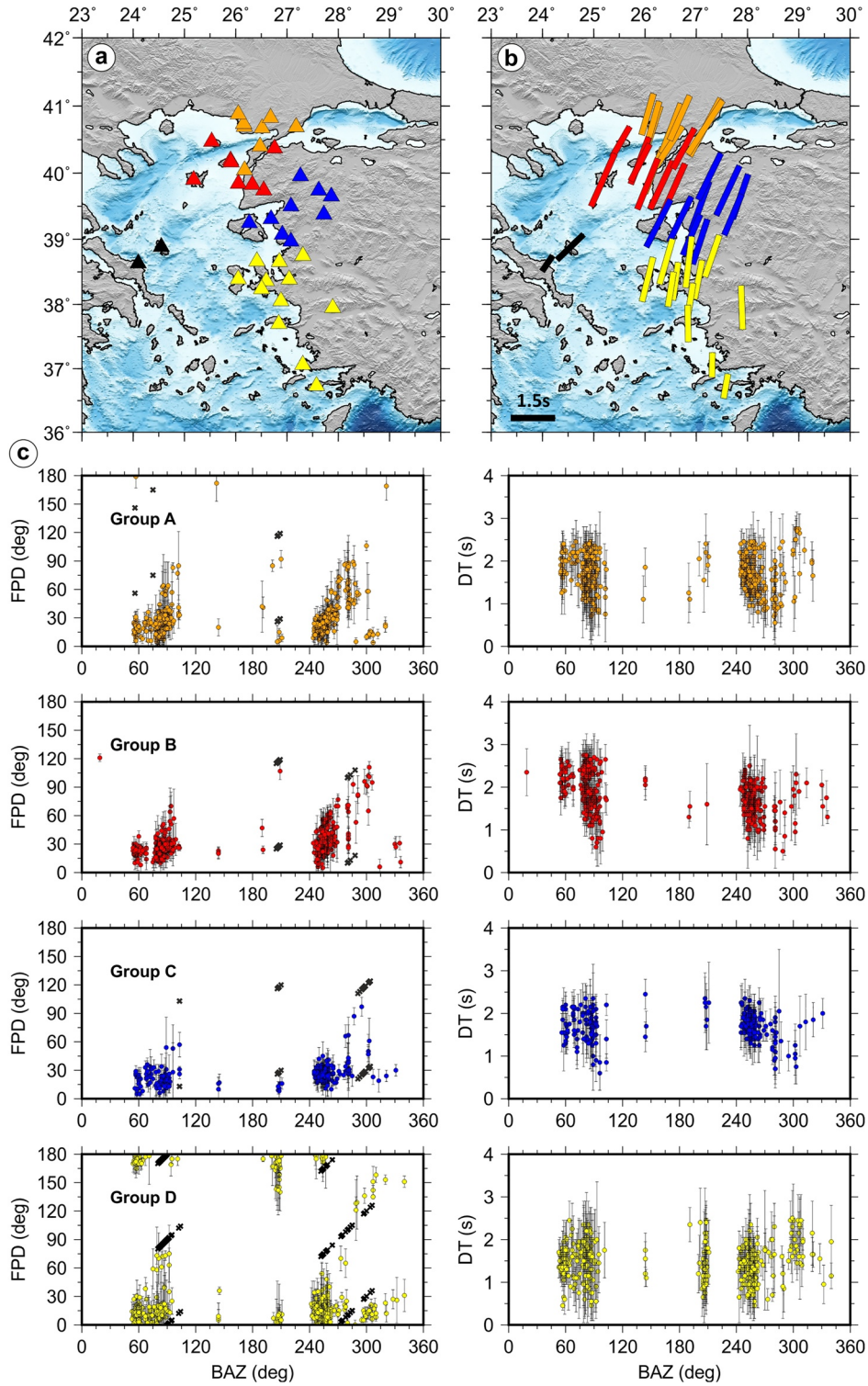

Figure 4. (a) Spatial distribution of the seismic stations grouped considering their locations is shown with orange (Thrace Basin), red (Rhodope-Strandja Massif), blue (Sakarya Zone), and yellow (Anatolide-Tauride Block) triangles. KYMI and SKY stations in the western Aegean are shown with black triangles and are not included in any group. (b) Averaged splitting parameters (fast polarization direction and Delay Time) derived from TE method are shown with bars that colored with the group they belong to. (c) Back-azimuthal variations of all individual splitting parameters into 4 main groups of stations. All individual null measurements are marked with black crosses.

Table 1

Station-Averaged SKS Splitting Parameters With Their Uncertainties Estimated From Both EV (Eigenvalue; Measured With Code by Teanby et al., 2004) and TE (Transverse Energy Minimization; Measured With "Multisplit") Methods

		EV			TE		
Group label	Station code	FPD (°)	DT (s)	#	FPD (°)	DT (s)	#
A	ALN*	7 ± 7	1.81 ± 0.16	188	16 ± 4	1.45 ± 0.20	188
	CAVK	13 ± 5	1.56 ± 0.11	22	18 ± 4	1.50 ± 0.10	15
	ECEA	17 ± 7	1.69 ± 0.13	27	21 ± 2	1.65 ± 0.10	17
	ENEZ*	7 ± 6	1.67 ± 0.12	30	16 ± 4	1.60 ± 0.20	38
	ERIK*	25 ± 6	1.69 ± 0.13	50	21 ± 2	1.80 ± 0.15	64
	GELI*	41 ± 6	1.89 ± 0.12	61	33 ± 3	1.65 ± 0.15	44
	KESN	39 ± 7	1.72 ± 0.17	30	24 ± 3	1.65 ± 0.15	19
	RKY*	33 ± 4	2.14 ± 0.10	78	28 ± 2	2.20 ± 0.10	95
	SART	46 ± 6	2.07 ± 0.13	18	33 ± 3	2.15 ± 0.20	10
B	BAYC*	25 ± 6	1.72 ± 0.13	38	24 ± 3	2.00 ± 0.15	31
	BOZC	23 ± 5	1.82 ± 0.14	38	22 ± 3	1.85 ± 0.15	21
	EZN	36 ± 7	1.62 ± 0.15	46	25 ± 2	1.80 ± 0.15	53
	GADA*	18 ± 6	1.76 ± 0.14	51	21 ± 4	1.70 ± 0.20	57
	GOAD	24 ± 5	1.99 ± 0.10	5	27 ± 4	1.40 ± 0.15	3
	LAP*	28 ± 7	1.66 ± 0.12	61	28 ± 4	1.55 ± 0.15	80
	LIA	36 ± 5	2.05 ± 0.15	146	24 ± 4	1.95 ± 0.20	146
	SMTH*	0 ± 6	1.43 ± 0.14	60	30 ± 7	1.20 ± 0.15	29
C	AYVA	22 ± 6	1.87 ± 0.17	40	26 ± 3	1.70 ± 0.15	32
	BALB	23 ± 6	1.62 ± 0.16	48	19 ± 3	1.60 ± 0.15	60
	BALY	26 ± 6	1.76 ± 0.16	46	25 ± 3	1.85 ± 0.10	32
	BUHA	15 ± 5	1.78 ± 0.13	47	20 ± 2	1.80 ± 0.15	27
	DKL*	18 ± 6	1.61 ± 0.15	42	23 ± 4	1.50 ± 0.25	35
	NEV	32 ± 5	1.71 ± 0.13	39	26 ± 3	1.75 ± 0.15	22
	PRK	28 ± 4	1.81 ± 0.10	73	27 ± 3	1.80 ± 0.10	43
	STEP	14 ± 5	1.12 ± 0.16	15	23 ± 4	1.50 ± 0.15	14
	ZEDA	22 ± 5	1.51 ± 0.12	36	18 ± 3	1.60 ± 0.15	18
D	AYDB	155 ± 5	1.35 ± 0.15	19	178 ± 4	1.50 ± 0.15	19
	BAG	12 ± 5	1.83 ± 0.14	10	7 ± 5	1.75 ± 0.30	7
	BLCB	19 ± 7	1.46 ± 0.16	33	11 ± 3	1.35 ± 0.20	34
	BODT	13 ± 8	1.05 ± 0.16	18	1 ± 8	0.85 ± 0.20	21
	CAM	22 ± 6	1.52 ± 0.12	6	19 ± 4	1.50 ± 0.15	5
	CHOS	28 ± 7	1.38 ± 0.15	166	14 ± 3	1.55 ± 0.15	166
	DAT	10 ± 9	1.25 ± 0.20	25	10 ± 4	0.85 ± 0.10	29
	DGB*	22 ± 7	1.33 ± 0.15	30	9 ± 4	1.25 ± 0.15	18
	KARB	10 ± 5	1.63 ± 0.12	16	16 ± 3	1.60 ± 0.10	12
	SMG*	178 ± 9	1.57 ± 0.23	108	179 ± 4	1.25 ± 0.15	108
	URLA*	14 ± 6	1.28 ± 0.14	22	8 ± 4	1.30 ± 0.15	16
	ZEYE*	8 ± 6	1.29 ± 0.12	32	9 ± 5	1.20 ± 0.15	20
	KYMI	18 ± 11	0.95 ± 0.23	15	34 ± 8	0.65 ± 0.10	3
	SKY	38 ± 8	1.36 ± 0.16	25	46 ± 5	1.25 ± 0.20	9

Note. The number of SKS measurements (#) is also given. *possible two-layer anisotropy beneath these stations.

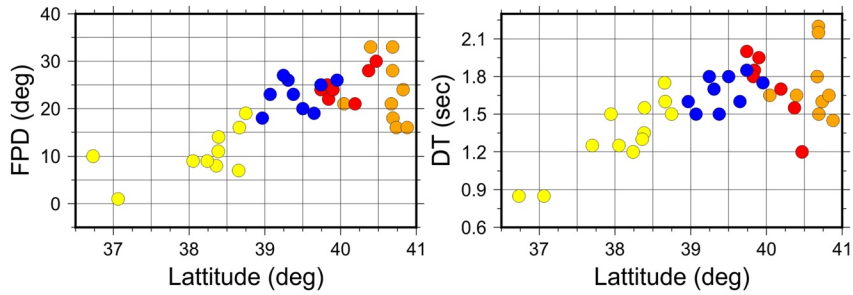

Figure 5. Latitude-dependent variations of average splitting parameters of 38 seismic stations along western Anatolia. KYMI and SKY stations located in mainland Greece and the western Aegean are not included. Circles represent the average splitting parameters of stations and colored by the groups to which they belong (see Results section and Figure 4 for details about the groups).

4.2. Null Measurements

Figure 3b presents an example of a clear null split observation from the 21 December 2016 earthquake (M_w 6.7) recorded at station DGB. Null splitting usually occurs when an event with SKS phase arrive at the station from back-azimuths nearly parallel or perpendicular to the fast or slow back-azimuths resulting in the absence of energy on tangential components. In total, we acquired 137 good null splits beneath 26 seismic stations. Back-azimuths of the events with these clear null measurements are nearly (within maximum ±12° discrepancy) consistent with the station-averaged fast and/or slow polarization directions except for 7 stations (BLCB, BODT, DAT, KYMI, RKY, SART, and SKY) as can be seen in Figure S2 in Supporting Information S1. For station KYMI we noticed an evident scattered distribution of backazimuths null events. The majority of the null observations (115 out of 137) were observed for the events approaching from back azimuths almost in-line with the inferred slow axes of anisotropic orientation from good splitting measurements. Back-azimuths of the events with the detected null splitting examples range between 250°–306° (for 60 null splits) and 80°–105° (for 55 null splits) (Figure S6 in Supporting Information S1).

4.3. Two-Layer Anisotropy Observations

The directional dependence of individual apparent splitting estimates inferred from both TE and EV approaches and rose diagrams of the FPD values scaled by DT values at 40 stations enabled a first-order approximation for our understanding whether more complicated anisotropic structure (e.g., two-layer anisotropy) exists beneath the given station. We noticed that for many stations the FPDs and DTs exhibited a notable variation with back-azimuths (Figures S1 and S2 in Supporting Information S1), implying a more complex anisotropic structure rather than a simple single-layer in the upper mantle, in particular beneath NW Anatolia (Figure 6). Systematic backazimuth dependent variations of FPDs and DTs are also visible in the summary plots in Figure 4b, as described in Section 3.1 Furthermore, signs of two-layer behavior at selected stations are noticeable in Figure S7 in Supporting Information S1 where the lateral variation of all individual FPDs estimates is shown as color coded by their corresponding anisotropic orientation and are projected to the surface based on ray-piercing points at the 100 km depth.

We investigate possible two-layer anisotropy parameters beneath 14 stations (ALN, BAYC, DGB, DKL, ENEZ, ERIK, GADA, GELI, LAP, RKY, SMG, SMTH, URLA, and ZEYE). Our findings from the grid search approach suggest two-layer models with well-defined splitting parameters explain the azimuthal patterns beneath BAYC, GADA, ERIK, LAP, and RKY. For the stations for which we could not obtain reliable two-layer models with the grid search approach (DGB, DKL, ENEZ, GELI, SMTH, URLA, and ZEYE), the curve fitting approach gave fairly reliable two-layer models with $R^* \geq 0.45$. Since the number of events is not sufficient to investigate two-layer splitting anisotropy parameters separately at closely located stations DGB, URLA, and ZEYE we obtained a composite two-layer model by merging 54 individual event splitting parameter estimates from these three stations. We note that our individual apparent single-layer splitting parameters are in a good accordance with two-layer theoretical curves calculated based on the theoretical framework in Silver and Savage (1994) and, in particular, exhibit a back-azimuthal variation with π/2 periodicity (Figure 7a). The preferred two-layer models derived from grid search and curve-fitting approaches for 14 seismic stations are summarized in Table 2.

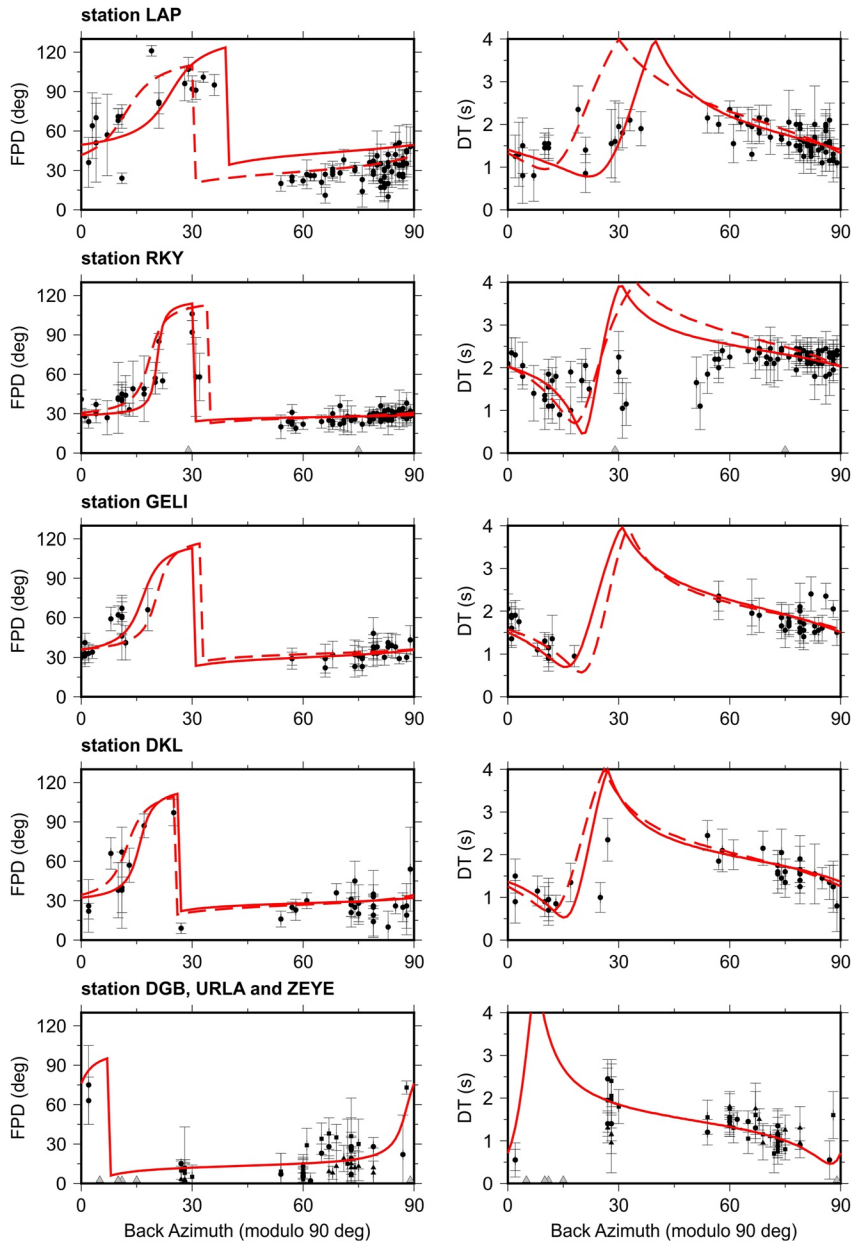

Figure 6. Comparison of predicted and observed apparent splitting parameters for final two-layer models derived from curve fitting (solid line) and two-layer grid search (dashed line) approaches. Closely located 3 stations DGB, URLA, and ZEYE stations are plotted together in last row.

We tested the grid search results with a jackknife test over different sub-data sets, which generally revealed two-layer parameters for each realization distributed close to the grid search-derived optimal two-layer parameters, demonstrating the robustness of the estimate (Figure 7b). Generally speaking, both grid search and curve fitting approaches resulted in consistent two-layer models. As an example, for station LAP, we obtained two-layer splitting parameters from grid search as FPD_{upper}: 65°, DT_{upper}: 0.9 s, FPD_{lower}: 10°, DT_{lower}: 2.15 s, with standard deviations of the four parameters (Figure 7). Similarly, curve fitting approach resulted in two-layer model parameters as FPD_{upper}: 72°, DT_{upper}: 0.8 s, FPD_{lower}: 20°, DT_{lower}: 1.5 s for this station.

The obtained final two-layer models showed that the FPDs are between N22°E and N72°E, and between N6°W and N20°E for the upper and lower layers, respectively. The estimated DTs range from 0.6 to 2.0 s and from 0.6

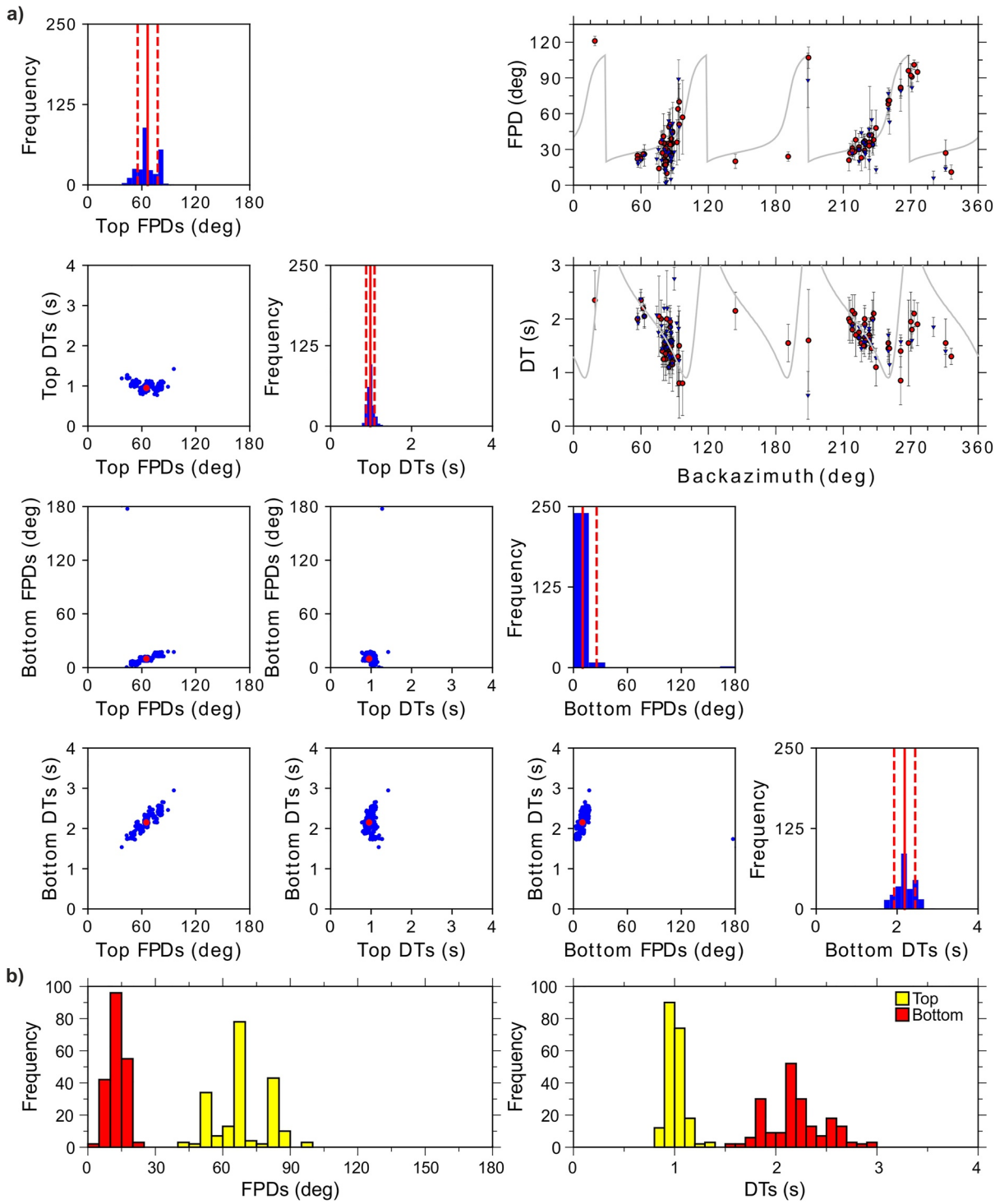

Figure 7. (a) Scatter plots to assess the pair-wise trade-offs between all possible combinations of four two-layer anisotropic parameters based on bootstrap sampling at example station LAP. Red dot shows the estimated fast polarization directions (FPDs) and Delay Time (DT) of final two-layer anisotropy parameters derived from stacking of 61 error surfaces obtained from two-layer grid search of a total of 61 events. Small blue dots present two-layer model parameters that are estimated from 250 bootstrap realizations. Corresponding histograms for each parameter are shown on the main diagonal. Red solid line in each histogram represents final model and dashed lines show corresponding standard deviation of the bootstrap sample. Back-azimuthal variations of individual FPD and DT measurements obtained from TE and EV methods are represented with red circles and blue triangles, respectively, in two rectangle boxes at the right top. Gray lines in two rectangle boxes represent two-layer curve for the model derived by two-layer grid search. (b) Histograms show the distribution of FPDs and DTs for upper (yellow) and lower (red) layers derived by using 200 randomly selected data sets.

Table 2
Two-Layer Model Parameters for 14 Seismic Stations Obtained From Both Curve Fitting and Two-Layer Grid Search Approach

	Two-layer grid search				Curve fitting				
Seismic stations	FPD_{upper} (°)	DT_{upper} (s)	FPD_{lower} (°)	DT_{lower} (s)	FPD_{upper} (°)	DT_{upper} (s)	FPD_{lower} (°)	DT_{lower} (s)	*R**
LAP	**65**	**0.95**	**10**	**2.15**	72	0.8	20	1.5	0.60
GELI	40	1.2	10	1.0	**53**	**0.8**	**13**	**1.7**	**0.45**
GADA	**55**	**0.6**	**10**	**2.0**	40	0.6	10	1.6	0.57
RKY	**35**	**1.55**	**10**	**1.3**	29	2.0	1	0.6	0.63
BAYC	**35**	**1.35**	**5**	**1.2**	56	0.3	17	2.0	0.17
ERIK	**25**	**1.5**	**0**	**0.90**	32	1.3	2	1.1	0.23
DKL	45	0.7	10	1.4	**42**	**0.8**	**11**	**1.3**	**0.55**
SMTH	95	1.75	15	3.0	**62**	**0.8**	**5**	**1.7**	**0.46**
ENEZ	85	1.25	10	2.9	**22**	**0.9**	**10**	**0.9**	**0.47**
ALN	85	0.8	10	2.4	**36**	**0.7**	**0**	**1.6**	**0.64**
SMG	–	–	–	–	**18**	**0.7**	**−15**	**1**	**0.89**
DGB									
URLA	–	–	–	–	**30**	**0.6**	**−6**	**1.1**	**0.75**
ZEYE									

Note. Gray shaded models derived from two-layer grid search have relatively large variations while green shaded models have good convergence to the final two-layer model. The models marked in bold were used for final interpretations.

to 2.15 s in the upper and lower layer, respectively. The spatial distributions of both averaged single-layer and selected plausible two-layer anisotropy models are summarized in Figure 8.

The average of the FPDs estimated for the upper layer at four stations including GADA (N55°E), GELI (N53°E), LAP (N65°E) and SMTH (N62°E) which are closely located to the NAFZ (Figure 8), is ∼N60°E, which is sub-parallel to the strike of this fault zone. The DT estimates for a possible upper layer at the stations GADA and SMTH (North Aegean Sea) are 0.6 and 0.8 s, respectively. Other three stations, that is, ENEZ, ERIK and RKY, located at the north of the NAFZ, have an average upper layer FPD with approximately ∼N27°E orientation, that is, oblique with respect to the NAFZ. Among these stations, the largest upper layer DTs (about 1.5 s) are measured for stations ERIK and RKY. Overall NNE-SSW FPDs with an average of ∼N8°E in the lower layer were estimated for these seven stations located around closest to the NAFZ (Table 2 and Figure 8). In the southern part of the study area, the lower layer FPDs evidently indicate an NNE-SSW pattern, similar to the more northern stations.

5. Discussion

The use of various permanent broadband seismic stations enabled a comprehensive analysis on directional dependence of SKS splitting parameters, and thus, in particular helped to detect the signature of two-layer anisotropy. A noticeable two-layer anisotropy behavior of SKS phases sampling the upper mantle of some parts of the study region is one of the most important findings of this study. Depending on the azimuthal coverage and quality of the analyzed data, we grouped the stations into three category before the interpretation, such as, (a) stations with good azimuthal coverage used to solve for two-layer anisotropic structure (e.g., LAP), (b) stations with insufficient back-azimuthal distribution and/or noisy data to determine two-layer model (e.g., EZN), and (c) the stations with a solid evidence of the single layer anisotropy (e.g., BALY), in that azimuthal coverage is good enough to have detected two-layer splitting if it is present (Figure 8). We analyzed *P*-wave polarizations to understand whether considerably large differences between station-averaged FPDs estimated from the EV and TE methods at stations SMTH and AYDB are associated to possible sensor misorientations. However, our results reveal the negligible effect of sensor misorientations. Earlier Vecsey et al. (2008) have reported TE-derived FPDs

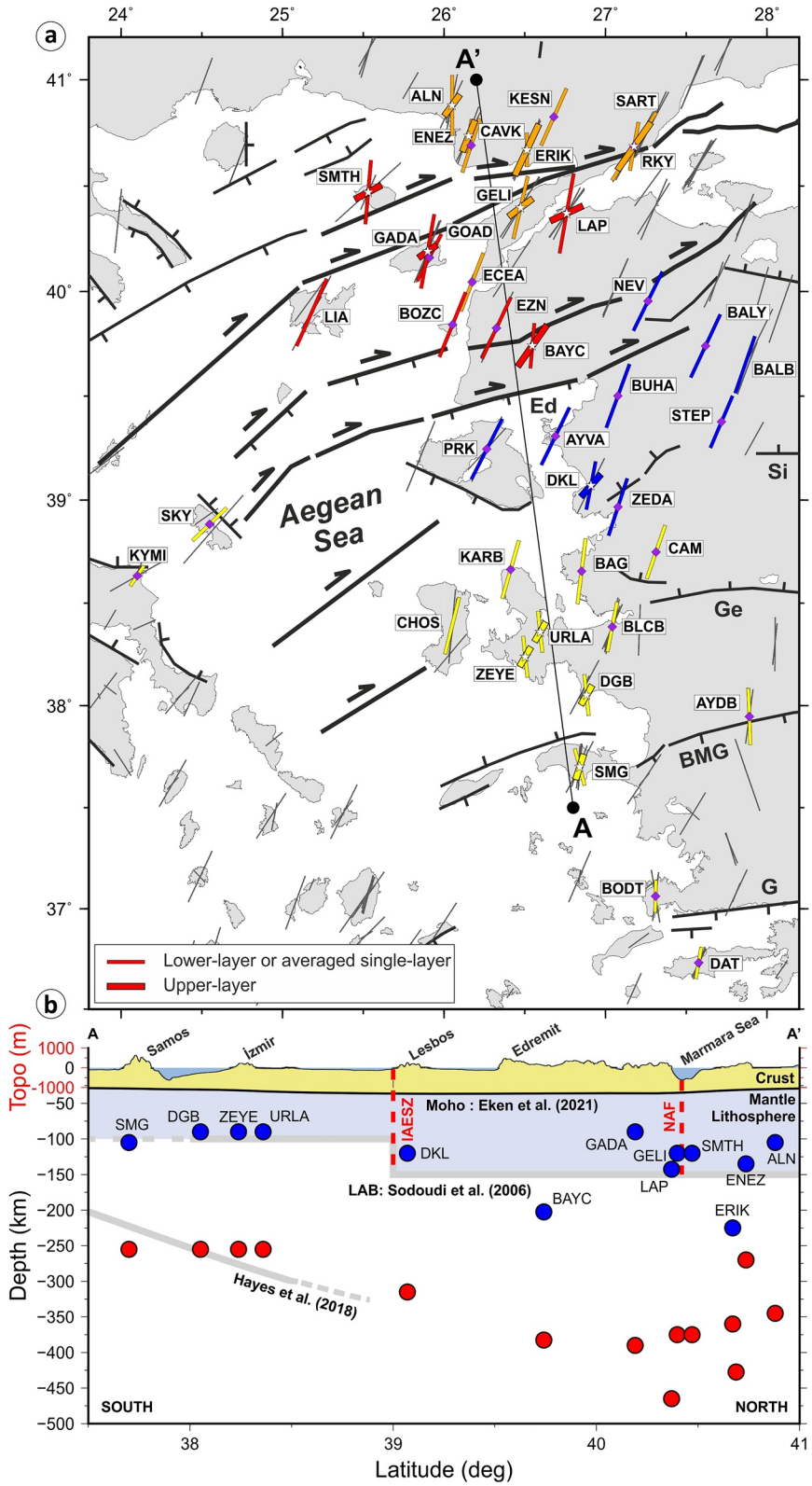

Figure 8.

would be more stable compared to EV-derived once under the presence of noisy SKS phase conditions as their numerical tests can explain significant deviations between these two methods for stations SMTH and AYDB in this study. Below we discuss and interpret main outcomes of this study.

5.1. Implications of Double Layer Anisotropy

5.1.1. Lithospheric Anisotropy Near the Western NAFZ and Central-Westernmost Anatolia

To the northwest, for three stations located just south of the NAFZ (GADA, GELI, and LAP) and station SMTH located just north of the NAFZ in the North Aegean Sea, we noticed upper layer FPDs are quite compatible with the strike of this lithospheric scale strike-slip fault. This consistency favors the idea of a lithospheric continuation of the right-lateral shear deformation beneath NW Anatolia. This observation is further supported by previous geodetic studies (e.g., Hollenstein et al., 2006; McClusky et al., 2000, 2003) that have explained the velocity field in the eastern Mediterranean by a major block of bounding faults (e.g., NAFZ/NAT, CTF, and EAFZ) implying a localization of shear deformation also in the mantle lithosphere below these faults (Figure 1).

The average DT of the upper layer for these 4 stations is ∼0.8 s which may arise from a ∼90 km thick layer with an assumption of 4% anisotropy. On the other hand, we estimated both fault-oblique FPDs (NNE-SSW; approximately ∼N27°E) and relatively larger DTs (∼1.3 s) for the upper layer of three stations (ENEZ, ERIK RKY) located at the north of NAF. This indicates the asymmetry in where the more distributed deformation in the mantle lithosphere occurs, that is, the Anatolia block is exposed to rapid active deformation with respect to Eurasia to the north of the NAFZ. For the western segment of the NAF, Biryol et al. (2011) confirms our observations on mantle lithosphere by reporting abrupt thinning of the lithosphere from north to south. They proposed the NAF-related deformation might extend through the entire crust and penetrate into the uppermost mantle.

Several seismic imaging studies revealed a relatively thin lithospheric thickness (e.g., 80–100 km) beneath most parts of western Anatolia (e.g., Kind et al., 2015; Piromallo & Morelli, 2003; Salaün et al., 2012). However, a locally thicker lithosphere of about 130 km thickness beneath NW Anatolia was found by many different seismic tomography studies (e.g., Biryol et al., 2011; Confal et al., 2020; Konoudis et al., 2020; Portner et al., 2018; Salaün et al., 2012), with the Izmir-Ankara-Erzincan Suture Zone (IAESZ) marking the southern boundary of this fast velocity anomaly (Portner et al., 2018). An even more extreme south-to-north thickening of mantle lithosphere has been estimated by Artemieva and Shulgin (2019) who proposed an abrupt increase in the lithospheric thickness from the Menderes Massif (MM; 60–80 km) in the south to the SZ in the north (140–160 km). The decrease of upper layer DT from 1.35 s for the station in the SZ (BAYC) to 0.8 s near the IAESZ (DKL) and finally 0.6 s in the MM (joint DGB, URLA, ZEYE), corresponding to ∼150, 90, and 68 km thick anisotropic upper layer, respectively, presumably reflects at least qualitatively the abrupt thinning in the lithospheric thickness. The apparent difference between our lithospheric thickness estimate associated to the anisotropic upper layer and those mainly derived from seismological constraints in NW Anatolia can be easily reconciled by accounting for uncertainties in the average DT and pre-existing lithospheric thickness estimates, and minor variations in the assumed anisotropic strength. Furthermore, the seismological estimates include the crust, which will only contribute slightly to the DT.

We further investigated the depth extent of lithospheric structure through harmonic decomposition performed on receiver functions (RFs) (e.g., Licciardi et al., 2018; see Text S1 and Figures S10–S13 in Supporting Information S1 for further details) at station SMTH that is located in a close proximity to the NAT in the northern Aegean (Figure 1b). The amplitude of the anisotropic term in the harmonic time series reveals a relatively strong

Figure 8. (a) Map of the averaged single-layer and two-layer splitting results of 40 stations, with the main tectonic structures in western Anatolia. Splitting results obtained in this study are represented with bars colored by considering their locations (see Figure 4 and Text for details). Upper layer anisotropy is shown with thick bars and the thicker frames while lower layer and averaged single layer anisotropy results are represented with thin bars. White stars mark the stations that we present the two-layer anisotropy model, while purple diamonds indicate the stations that have insufficient back-azimuthal distribution and/or noisy data to determine the two-layer model, so we provide average single layer splitting parameters for these stations. Averaged splitting parameters of previous studies (Confal et al., 2016; Evangelidis, 2017; Evangelidis et al., 2011; Hatzfeld et al., 2001; Kaviris et al., 2018; Olive et al., 2014; Paul et al., 2014; Schmid et al., 2004; Vinnik et al., 1992) are showing with the thin gray bars (b) Depth cross section along the black line from A to A' in (a). Blue and red circles represent estimates of the bottom depths of upper and lower anisotropic layers, respectively, which are calculated by converting the corresponding delay times to layer thickness assuming a 3% anisotropy, and further assuming that the upper layer reaches to the surface. The bottom of the upper anisotropic layer approximately mirrors the changes in Lithosphere-Asthenosphere Boundary depth reported by Sodoudi et al. (2006), while the bottom of the lower anisotropic layer matches the top of the subducted African lithosphere in the southern portion of the profile, according to SLAB2.0 model of Hayes et al. (2018). Abbreviations: IAESZ: Izmir-Ankara-Erzincan Suture Zone; NAF: North Anatolian Fault.

anisotropic nature of the mantle lithosphere compared to the crust beneath station SMTH implying LPO is strong in the mantle lithosphere but not in the crust. The anisotropic orientation representing the lithospheric average was estimated as N152°E indicating either the fast or slow axis. Distinguishing these possibilities from RFs would require further analysis. However, the SKS-derived upper layer FPD for SMTH in this study is oriented nearly at right angles to this direction (N62°E), showing that the anisotropic orientation inferred from harmonic decomposition of receiver functions corresponds to the slow axis. The anisotropic orientations estimated from RFs analysis additionally confirms the continuation of the NAFZ to lithospheric depths in this part of the fault zone. Specifically, the harmonic analysis revealed ∼31 and 138 km for the Moho and lithospheric thicknesses, respectively. This confirms our earlier assessment of the source of upper layer anisotropy in the lithosphere. To summarize, we interpret the lithospheric fabric as the effect of right lateral deformation inside the mantle lithosphere at the western end of the NAFZ where the fault zone meets large back-arc extension.

5.1.2. Asthenospheric Anisotropy in East Aegean and Western Anatolia

The estimated lower layer FPDs varying between N-S and NNE-SSW oriented fast shear wave azimuths ranging from N6°W to N13°E and relatively large lower layer DTs (up to 2.15 s; average ∼1.5 s), in general, can be interpreted as a signature of the strain-induced LPO of olivine crystals (e.g., Babuška & Cara, 1991). The LPO in this region likely develops due to mantle flow induced by the roll-back of subducting African slab and mostly causes fast axis aligning with the direction of maximum extension for shear deformation (Figures 9 and 10). Similar to the station average single layer FPDs we observe a southward trend for counter-clockwise rotation of lower layer FPDs. Such variation pattern brings additional support to the perturbing effect of asthenospheric material entrainment through slab tear beneath southwestern Turkey on the mantle flow dynamics in the region that has been proposed in early studies (e.g., Biryol et al., 2011; Confal et al., 2020; Paul et al., 2014). Influence of the rapid change in lithospheric thickness at IAESZ on mantle flow field (e.g., edge-driven flow; see King & Anderson, 1998; Kaislaniemi and van Hunen, 2014) may be another possible explanation to counter-clockwise rotation of single-layer FPDs and lower layer FPDs from north to south. Further we compared our lower-layer anisotropy results with the absolute plate motion model (NNR-MORVEL-56; Argus et al., 2011), which describes the current motion of 56 plates relative to no-net-rotation (NNR) reference frame, and we noticed quite large discrepancies between the estimated lower-layer FPDs and NNR-based absolute plate motion (APM) beneath western Anatolia (Figure 9a). This evidences a more heterogeneous pattern of anisotropy that cannot be explained by a simple asthenospheric flow beneath the region. The observed large discrepancy then is due to the apparent abrupt variations in lithospheric thickness across study area, which are expected to possibly alter the asthenospheric flow (Bormann et al., 1996; Kaviani et al., 2009) and result in a large deviation from the APM flow.

Furthermore, relatively scattered nulls, in particular at the western Aegean (e.g., station KYMI, near the Corinth Rift) with limited good non-null measurements (Figures S1e and S2e in Supporting Information S1) might be correlated with (a) the noise or waveform complexity for the stations in this area (Vecsey et al., 2008) or (b) complex mantle flow around the subduction zones. Previous studies (e.g., Evangelidis, 2017; Olive et al., 2014) proposed that there is a transition from trench parallel to trench normal FPDs around the Corinth rift at the western end of the Hellenic arc. A complex asthenospheric flow in the mantle wedge may lead to the scattered nulls from the SKS phases which propagate into the anisotropic domains with trench normal and trench perpendicular FPDs beneath the KYMI station (Figure 2a).

5.2. The Origin of the Anisotropy

We mainly estimate NE-SW FPDs and DTs between 0.65 and 2.2 s (Figure 4b). The integrated strength of seismic anisotropy in the upper mantle can result in large DTs up to 3 s observed in global-scale (Savage, 1999), while crustal anisotropy usually contributes only about 0.1–0.2 s (Crampin, 1994). The magnitude of our DTs thus implies that the origin of observed seismic anisotropy can be mostly explained by a combined effect of an internal deformation of the mantle lithosphere and/or asthenosphere (Figure 9). Mean DTs are systematically increasing from south to north; starting with 1.33 s (group D) in the south, there is a strong gradient across the IAESZ to 1.68 s for groups C and B, respectively, and then a more gradual further increase 1.74 s for group A in the neighborhood of the NAFZ in the north of the study region (Figures 4 and 8). Assuming an anisotropic strength of 4% and a mantle S velocity of 4.5 km/s, the large DTs in the northern Aegean and northern West-Anatolia imply a 190–200 km thick anisotropic layer. As we mentioned in Section 4.1, seismic imaging studies mainly revealed thick lithosphere (∼130 km) for NW Anatolia and stepwise lithospheric thickening at IAESZ (e.g., Biryol

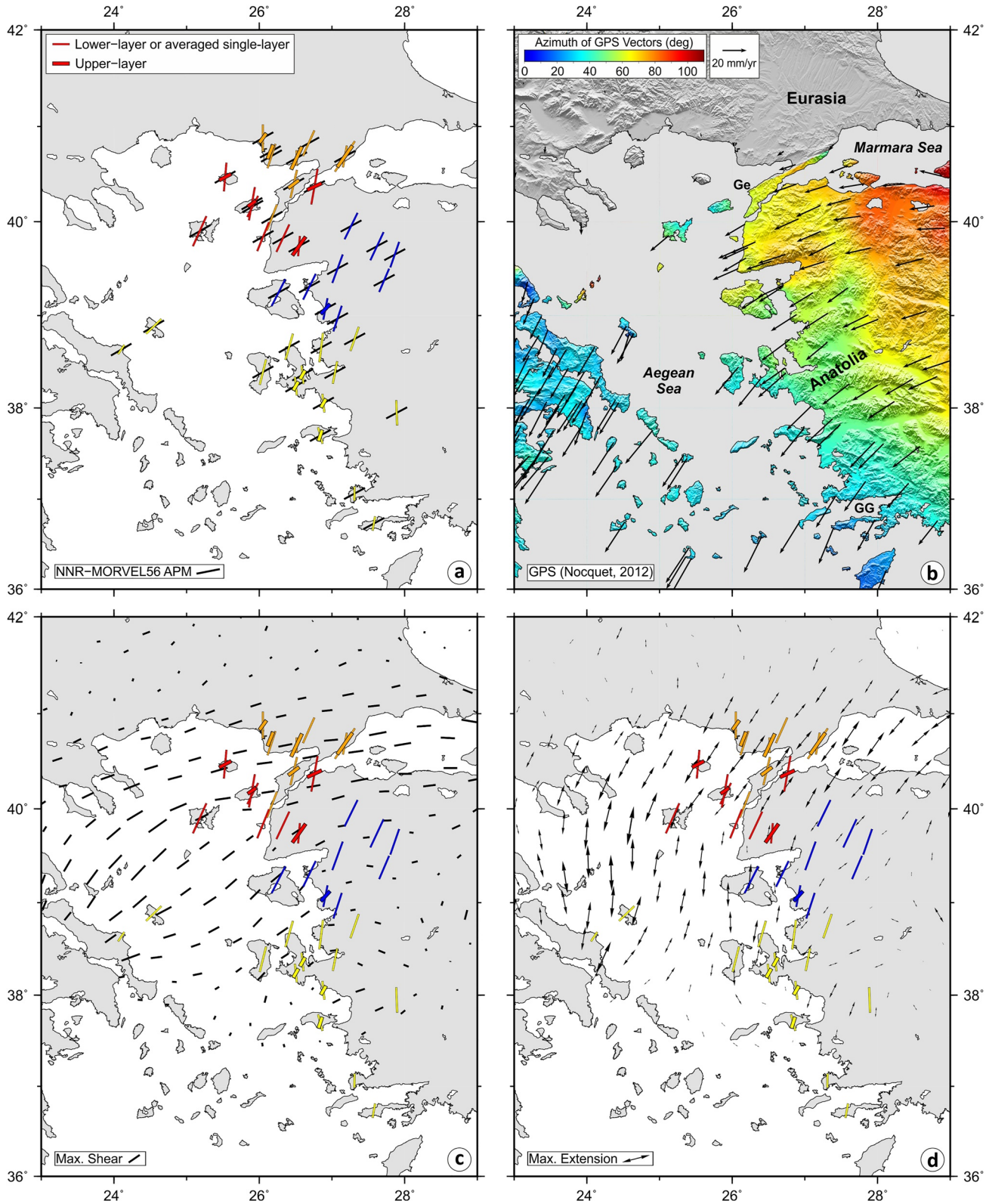

Figure 9. Comparison of anisotropy results with the (a) absolute plate motion relative to no-net rotation (NNR) reference frame (using NNR-MORVEL56 model from Argus et al., 2011), (b) geodetic observations from Nocquet (2012), and maximum shear (c) and maximum extension (d) directions that reported by Barbot and Weiss (2021) by evaluating the geodetic observations.

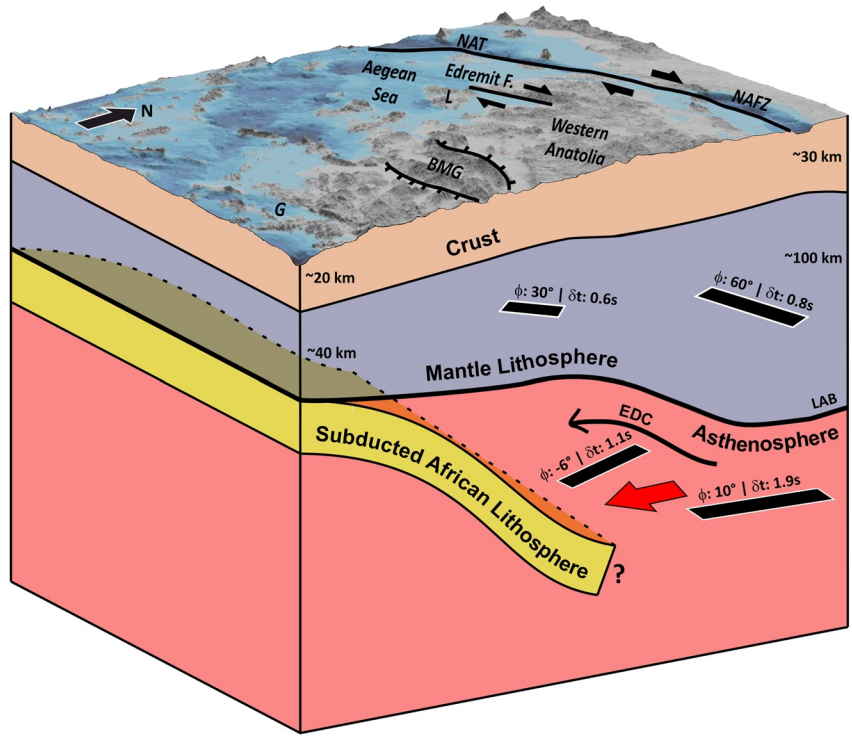

Figure 10. 3D illustration of two-layer anisotropy model proposed in this study in relation to the geodynamic setting of the Aegean and western Anatolian region. The Moho depth values and Lithosphere-Asthenosphere Boundary were from Vanacore et al. (2013), Portner et al. (2018), Artemieva and Shulgin (2019) and Confal et al. (2020), respectively. The depth of the subducted African lithosphere was taken from the SLAB2.0 model of Hayes et al. (2018). Abbreviations: BMG: Büyük Menderes Graben; EDC: Edge-driven convection; EFZ: Edremit Fault Zone; G: Gulf of Gökova; L: Lesvos Island; NAFZ: North Anatolian Fault Zone; NAT: North Aegean Through. Black bars indicate fast polarization directions scaled with time delays for two-layer model. Red arrow represents the direction of mantle flow induced by roll-back of subducted African lithosphere. SRTM 15+ topography data is plotted with 5 times vertical exaggeration.

et al., 2011; Confal et al., 2020; Konoudis et al., 2020; Portner et al., 2018; Salaün et al., 2012). Considering the substantial discrepancy between even relatively thick lithosphere and estimated anisotropic layer thickness in the north it is clear that a purely lithospheric origin can be excluded. A substantial decrease in DT across the IAESZ further agrees spatially with an abrupt decrease of lithospheric thickness at the same spot. This qualitatively implies that the contribution of the asthenosphere is, on a regional level similar in the north and south, that is, that the much smaller DT that can accumulate in the thinner lithosphere in the south is not compensated by a thicker anisotropic layer in the asthenosphere.

5.3. Comparison With Plate Kinematics and Strain Field

An obvious counter-clockwise rotation in FPDs from the north (N23–25°E for Groups A–C) to the south (N8°E for Group D), with the transition again at or near the IAESZ might be related to the change in asthenospheric flow pattern when approaching toward the slab window at the eastern end of the Hellenic trench (Table 1; Figures 4, 5, and 8). Such a rotation in FPDs was earlier discussed in Paul et al. (2014), Lemnifi et al. (2017), and Confal et al. (2018) and we speculate that stepwise change in lithospheric thickness at the IAESZ may lead to edge-driven convection rotating the mantle flow as we discussed in section of asthenospheric anisotropy.

The GPS vectors trend highly obliquely to the FPDs, and exhibit a gradual counter-clockwise rotation of the rapid W-SW directed motion of the Anatolian-Aegean block relative to the fixed Eurasian Plate (e.g., Hollenstein et al., 2006; McClusky et al., 2000, 2003; Nocquet, 2012; Reilinger et al., 2006) (Figure 9b). The orientation of GPS vectors is about 65° around the Gelibolu Peninsula, and then changes to about 30° near the Gulf of Gökova (Figures 1c and 9b; Nocquet, 2012). Such rotations of blocks about both vertical and horizontal axes in the

Aegean was also extensively reported by paleomagnetic and seismological studies (Kissel & Laj, 1988; Taymaz et al., 1991).

A comparison of our two-layer and single-layer splitting parameters with maximum extension and maximum shear directions (Barbot & Weiss, 2021) indicates a clear consistency of upper layer FPDs with the maximum shear directions especially for the southern NAFZ. It implies vertically coherent deformation that simply refers the coupling between the crust and mantle lithosphere, except for the north of NAFZ (stations ENEZ, ERIK, and RKY). Furthermore, lower layer and single-layer anisotropy directions are comparable with maximum extension directions for the entire study region with the only exception at stations KYMI and SKY at the western Aegean Sea, reflecting the finite extensional strain developed due to the asthenospheric mantle flow (Figures 9c and 9d). These findings reveal the substantial effect of shear deformation along the NAFZ on anisotropic orientations particularly in the lithospheric mantle depths.

5.4. Lithospheric-Scale Shear Deformation Along the NAFZ Compared to Other Shear Deformation Zones

A broad data set of station average FPDs in several single-layer SKS splitting studies showed predominantly fault-parallel anisotropic orientations along large-scale lithospheric strike-slip fault zones, that is, the San Andreas Fault (SAF) in California (e.g., Bonnin et al., 2010; Polet & Kanamori, 2002), Kunlun, Altyn Tagh Faults in Tibet (e.g., Eken et al., 2013; Herquel et al., 1999; Leòn Soto et al., 2012), Talas-Fergana and Karakorum Faults in Pamir and Hindu Kush (e.g., Kufner et al., 2018), and Dead Sea Transform Fault in the Arabian Plate (Rümpker et al., 2003). They suggest strong control of these major faults on the deformation throughout the lithosphere (e.g., macroscopic fault structures).

Our findings on two-layer anisotropy nearby the northwestern end of the NAFZ can be considered analogous to those SWS measurements obtained along the ∼1,500 km long right-lateral SAF. In fact, the combined length of the NAFZ and NAT, starting from Karlıova triple junction in Eastern Anatolia and crossing the entire Anatolia and Aegean Sea is almost the same as the SAF. However, it is a younger strike-slip fault with a smaller offset (∼13–11 Ma and ∼80–90 km; Şengör et al., 1985, 2005) compared to many other lithospheric-scale transform faults (e.g., central SAF, ∼23 Ma and ∼315 km offset; Revenaugh & Reasoner, 1997). Polet and Kanamori (2002) proposed a two-layer anisotropy model, which consisted of an upper layer with FPDs parallel to the strike of SAF (∼N135°E) and with splitting time delay of ∼0.7 s, as expected for the lithospheric thickness in the region. Their estimated lower layer anisotropic parameters likely linking to an asthenospheric origin indicated an E-W fast wave orientation (parallel to the APM) with splitting time delay ∼1.4 s beneath the central part of SAF in California. In contrast, toward the central and eastern NAFZ, station-averaged single-layer SKS splitting parameters (e.g., Biryol et al., 2010; Paul et al., 2014) generally exhibited fault-oblique FPDs. More recently Lemnifi et al. (2017) and Merry et al. (2021) from directional dependence of SKS phases could not detect a clear signature of two-layer anisotropic structure at these parts of the NAFZ, east of our study region.

Here, the important question is whether the western part of NAFZ is the only portion on the entire fault zone that presents a two-layer anisotropy structure with evidence for shear localization on lithospheric-scale. If this is the fact, what is the possible geodynamic explanation of this phenomenon? Wang et al. (2020) at the central part of the NAFZ have imaged evident decoupling between the crust and lithospheric mantle as the NE–SW fast *P*-wave directions in the uppermost mantle in their anisotropic *P*-wave local earthquake tomography model were correlated with previous SKS FPDs (e.g., Biryol et al., 2010; Paul et al., 2014), but different from either the N-S fast *P*-wave directions in the lower crust of their model or the GPS-derived E-W maximum shear directions (Özeren, 2012; Özeren & Holt, 2010). Beneath central Anatolia, a seismic low velocity zone (LVZ) is prevalent in the lower crust and uppermost mantle (between 50 km and >100 km), which gradually merges into the shallow Anatolian asthenosphere (e.g., Delph et al., 2015; Fichtner, Saygin, et al., 2013, Fichtner, Trampert, et al., 2013; Wang et al., 2020). This broad LVZ likely evidences the presence of hot upwelling of asthenospheric material beneath the Central Anatolian Plateau that has been initiated due to the roll-back and break-off of the Cyprus slab (e.g., Fayon & Whitney, 2007) and appeared to be connected to the anomalously low-velocities of the Central Anatolian Volcanic Provinces between 100 and 200 km depths (Fichtner, Saygin, et al., 2013, Fichtner, Trampert, et al., 2013). A low velocity anomaly down to the uppermost mantle (32–45 km) is noticeable beneath the central NAFZ but does not extend to its western parts (e.g., Konoudis et al., 2020; Fichtner, Saygin, et al., 2013, Fichtner, Trampert, et al., 2013; Wang et al., 2020; Wei et al., 2019). The anomalous character of directionally dependent

receiver functions (e.g., Licciardi et al., 2018; Vinnik et al., 2016) in the central part of the NAFZ were explained by anisotropic behavior of the sub-Moho with typically peridotite-type rock containing melt with fast directions normal to the direction of shear in the mantle at around depths of 35–60 and 60–90 km, rather than parallel as usually inferred for shear flow. However, laboratory experiments conducted under low temperature and high stress conditions confirm this interpretation as they result in fast directions normal to the direction of flow in water-rich olivine (Jung & Karato, 2001) and molten peridotite (Holtzman et al., 2003). According to Karato et al. (2008) and Kohlstedt and Holtzman (2009), the strain would divide between the melt-enriched bands and melt-depleted lenses affecting the rock fabric and upper mantle anisotropy. Thus, this may explain the absence of fault-parallel FPDs within lithospheric layer at the central NAFZ where the deformation was not transferred coherently through the crust and sub-Moho structures.

6. Conclusions

In this study, we investigated lateral and vertical variations of seismic anisotropy parameters in the upper mantle beneath the eastern Aegean and western Anatolia based on shear wave splitting of SKS phases. In particular, additional data from new stations operated by AFAD increased our knowledge of lateral variations in upper mantle anisotropy beneath this region. For the stations located in northern geological units (TB, RSM, and SZ), we obtained NE-SW oriented FPDs (~N20°E) and large DTs (~1.7–1.8 s) on average when assuming a single anisotropic layer with horizontal axis of symmetry. To the south station-averaged FPDs for the stations in the ATB unit are oriented NNE-SSW with a step change at the IAESZ. Station-averaged DTs south of the IAESZ are significantly smaller (~1.3 s) implying a much thicker anisotropic layer north of the IAESZ.

Further, we were able to separate the anisotropy in the mantle lithosphere and asthenosphere by performing two-layer anisotropy analysis for selected stations with good backazimuthal coverage. The upper layer anisotropy for the stations located at the western end of the NAFZ indicates that shear deformation parallel to the surficial trend of the fault extends vertically throughout the mantle lithosphere at this part of the fault zone. This observation could be evidence of coupling between crust and the mantle lithosphere at this part of the fault. Further south, in central-western Anatolia, the NE-SW aligned FPDs in the upper layer is interpreted as resulting from finite strain in the lithosphere, that is, FPDs are corresponding to the maximum shear direction. Overall N-S FPDs (N6°W-N13°E) in the lower layer (asthenospheric layer) are likely associated to the mantle flow induced by trench retreat and slab roll-back along the Hellenic subduction zone. Finally, we tentatively suggest a future anisotropy study covering the entire NAF with a large and multi-scale data set to get a better understanding of the complex anisotropic pattern beneath the region.

Data Availability Statement

The IRIS Data Management Center (https://www.iris.edu/hq/) was used to access seismic waveforms and the United States Geological Survey (USGS) to obtain earthquake hypocentral details respectively. This work includes data from permanent FDSN networks KO (Kandilli Observatory and Earthquake Research Institute, Boğaziçi University, 1971; https://doi.org/10.7914/SN/KO), TU (Disaster and Emergency Management Authority, 1990; https://doi.org/10.7914/SN/TU), HL (National Observatory of Athens, Institute of Geodynamics, 1975; https://doi.org/10.7914/SN/HL) and HT (Aristotle University of Thessaloniki Seismological Network, 1981; https://doi.org/10.7914/SN/HT). Digital waveform recordings were retrieved from the web interfaces of the IRIS-DMC (https://ds.iris.edu/wilber3/find_event), (http://eida.koeri.boun.edu.tr/webinterface) and Earthquake Data Centre System of Turkey (AFAD-DDA; http://tdvm.afad.gov.tr/). Software packages of Generic Mapping Tools (GMT; Wessel & Smith, 1998) and GeoMapApp (http://www.geomapapp.org) were used to prepare some of the figures, Seismic Analysis Code (Goldstein et al., 2003; Goldstein & Snoke, 2005) to process the conventional earthquake data and TauP-Time (Kennett et al., 1995) software is used for calculating the theoretical arrival times of seismic phases. Automated Shear Wave Splitting algorithm (Teanby et al., 2004; given in https://mfast-package.geo.vuw.ac.nz) and MultiSplit algorithm (Eken et al., 2013; Eken & Tilmann, 2014; https://github.com/ftilmann/multisplit) were used for SKS analysis. M_Split software of Abgarmi and Arda Özacar (2017) was utilized for the modeling of two-layer anisotropic structure.

Acknowledgments
This study is a part of an ongoing Ph.D. thesis, by Ceyhun Erman. We would like to thank Istanbul Technical University Research Fund (ITU-BAP) Turkish National Scientific, Technological Foundation (TUBITAK), Turkish Academy of Science in the framework for Young Scientist Award Program (TUBA-GEBIP), The Science Academy, Turkey - Young Scientist Awards Program (BAGEP), and Alexander von Humboldt-Foundation (AvH) for their financial support. We would like to thank the Dr. Sylvain Barbot for providing GPS-derived strain directions in western Anatolia. We are grateful to the Editor Michael Bostock, the reviewer Christos Evangelidis and an anonymous reviewer for their valuable comments, constructive advice and suggestions of judicial reviews that resulted in significant improvement of this manuscript.

References

Abgarmi, B., & Arda Özacar, A. (2017). M-Split: A graphical user interface to analyze multilayered anisotropy from shear-wave splitting. *Seismological Research Letters*, *88*(4), 1146–1155. https://doi.org/10.1785/0220170020

Al-Lazki, A. I., Sandvol, E., Seber, D., Barazangi, M., Turkelli, N., & Mohamad, R. (2004). Pn tomographic imaging of mantle lid velocity and anisotropy at the junction of the Arabian, Eurasian and African plates. *Geophysical Journal International*, *158*(3), 1024–1040. https://doi.org/10.1111/j.1365-246X.2004.02355.x

Al-Lazki, A. I., Seber, D., Sandvol, E., Turkelli, N., Mohamad, R., & Barazangi, M. (2003). Tomographic Pn velocity and anisotropy structure beneath the Anatolian plateau (eastern Turkey) and the surrounding regions. *Geophysical Research Letters*, *30*(24), 4–7. https://doi.org/10.1029/2003GL017391

Argus, D. F., Gordon, R. G., & Demets, C. (2011). Geologically current motion of 56 plates relative to the no-net-rotation reference frame. *Geochemistry, Geophysics, Geosystems*, *12*(11), 1–13. https://doi.org/10.1029/2011GC003751

Aristotle University of Thessaloniki. (1981). Aristotle University of Thessaloniki Seismological Network [Dataset]. International Federation of Digital Seismograph Networks. https://doi.org/10.7914/SN/HT

Artemieva, I. M., & Shulgin, A. (2019). Geodynamics of Anatolia: Lithosphere thermal structure and thickness. *Tectonics*, *38*(12), 4465–4487. https://doi.org/10.1029/2019TC005594

Babuška, V., & Cara, M. (1991). *Seismic anisotropy in the Earth*. Kluwer Academic Publishers.

Barbot, S., & Weiss, J. R. (2021). Connecting subduction, extension and shear localization across the Aegean Sea and Anatolia. *Geophysical Journal International*, *226*, 422–445. https://doi.org/10.1093/gji/ggab078

Barka, A., & Reilinger, R. (1997). Active tectonics of the eastern Mediterranean region: Deduced from GPS, neotectonic and seismicity data. *Annals of Geophysics*, *40*(3), 587–610.

Biryol, C. B., Beck, S. L., Zandt, G., & Özacar, A. A. (2011). Segmented African lithosphere beneath the Anatolian region inferred from teleseismic P-wave tomography. *Geophysical Journal International*, *184*(3), 1037–1057. https://doi.org/10.1111/j.1365-246x.2010.04910.x

Biryol, C. B., Zandt, G., Beck, S. L., Ozacar, A. A., Adiyaman, H. E., & Gans, C. R. (2010). Shear wave splitting along a nascent plate boundary: The North Anatolian Fault Zone. *Geophysical Journal International*, *181*(3), 1201–1213. https://doi.org/10.1111/j.1365-246x.2010.04576.x

Bonnin, M., Barruol, G., & Bokelmann, G. H. R. (2010). Upper mantle deformation beneath the North American–Pacific plate boundary in California from SKS splitting. *Journal of Geophysical Research*, *115*(B4), 1–17. https://doi.org/10.1029/2009jb006438

Bormann, P., Grünthal, G., Kind, R., & Montag, H. (1996). Upper mantle anisotropy beneath central Europe from SKS wave splitting: Effects of absolute plate motion and lithosphere–asthenosphere boundary topography. *Journal of Geodynamics*, *22*(1–2), 11–32. https://doi.org/10.1016/0264-3707(96)00014-2

Brun, J. P., & Faccenna, C. (2008). Exhumation of high-pressure rocks driven by slab rollback. *Earth and Planetary Science Letters*, *272*(1–2), 1–7. https://doi.org/10.1016/j.epsl.2008.02.038

Büyükakpınar, P., Aktar, M., Maria Petersen, G., & Köseoğlu, A. (2021). Orientations of broadband stations of the KOERI Seismic Network (Turkey) from two independent methods: P - And Rayleigh-wave polarization. *Seismological Research Letters*, *92*(3), 1512–1521. https://doi.org/10.1785/0220200362

Cochran, E. S., Vidale, J. E., & Li, Y. G. (2003). Near-fault anisotropy following the Hector Mine earthquake. *Journal of Geophysical Research*, *108*(B9), 2436. https://doi.org/10.1029/2002jb002352

Confal, J. M., Bezada, M. J., Eken, T., Faccenda, M., Saygin, E., & Taymaz, T. (2020). Influence of upper mantle anisotropy on isotropic P-wave tomography images obtained in the eastern Mediterranean region. *Journal of Geophysical Research: Solid Earth*, *125*(8), 1–21. https://doi.org/10.1029/2019JB018559

Confal, J. M., Eken, T., Tilmann, F., Yolsal-Çevikbilen, S., Çubuk-Sabuncu, Y., Saygin, E., & Taymaz, T. (2016). Investigation of mantle kinematics beneath the Hellenic-subduction zone with teleseismic direct shear waves. *Physics of the Earth and Planetary Interiors*, *261*, 141–151. https://doi.org/10.1016/j.pepi.2016.10.012

Confal, J. M., Faccenda, M., Eken, T., & Taymaz, T. (2018). Numerical simulation of 3-D mantle flow evolution in subduction zone environments in relation to seismic anisotropy beneath the eastern Mediterranean region. *Earth and Planetary Science Letters*, *497*, 50–61. https://doi.org/10.1016/j.epsl.2018.06.005

Crampin, S. (1994). The fracture criticality of crustal rocks. *Geophysical Journal International*, *118*(2), 428–438. https://doi.org/10.1111/j.1365-246X.1994.tb03974.x

Çubuk-Sabuncu, Y., Taymaz, T., & Fichtner, A. (2017). 3-D crustal velocity structure of Western Turkey: Constraints from full-waveform tomography. *Physics of the Earth and Planetary Interiors*, *270*, 90–112. https://doi.org/10.1016/j.pepi.2017.06.014

Delph, J. R., Biryol, C. B., Beck, S. L., Zandt, G., & Ward, K. M. (2015). Shear wave velocity structure of the Anatolian Plate: Anomalously slow crust in southwestern Turkey. *Geophysical Journal International*, *202*(1), 261–276. https://doi.org/10.1093/gji/ggv141

Disaster and Emergency Management Authority. (1990). Turkish National Seismic Network. *Department of Earthquake, Disaster and Emergency Management Authority*. https://doi.org/10.7914/SN/TU

Eken, T., & Tilmann, F. (2014). The use of direct shear waves in quantifying seismic anisotropy: Exploiting regional arrays. *Bulletin of the Seismological Society of America*, *104*(6), 2644–2661. https://doi.org/10.1785/0120140020

Eken, T., Tilmann, F., Mechie, J., Zhao, W., Kind, R., Su, H., et al. (2013). Seismic anisotropy from SKS splitting beneath Northeastern Tibet. *Bulletin of the Seismological Society of America*, *103*(6), 3362–3371. https://doi.org/10.1785/0120130054

Endrun, B., Lebedev, S., Meier, T., Tirel, C., & Friederich, W. (2011). Complex layered deformation within the Aegean crust and mantle revealed by seismic anisotropy. *Nature Geoscience*, *4*(3), 203–207. https://doi.org/10.1038/ngeo1065

Evangelidis, C. P. (2017). Seismic anisotropy in the Hellenic subduction zone: Effects of slab segmentation and subslab mantle flow. *Earth and Planetary Science Letters*, *480*, 97–106. https://doi.org/10.1016/j.epsl.2017.10.003

Evangelidis, C. P., Liang, W.-T., Melis, N. S., & Konstantinou, K. I. (2011). Shear wave anisotropy beneath the Aegean inferred from SKS splitting observations. *Journal of Geophysical Research*, *116*(B04314), 1–14. https://doi.org/10.1029/2010jb007884

Fayon, A. K., & Whitney, D. L. (2007). Interpretation of tectonic versus magmatic processes for resetting apatite fission track ages in the Niğde massif, Turkey. *Tectonophysics*, *434*(1–4), 1–13. https://doi.org/10.1016/j.tecto.2007.01.003

Fichtner, A., Saygin, E., Taymaz, T., Cupillard, P., Capdeville, Y., & Trampert, J. (2013). The deep structure of the North Anatolian fault zone. *Earth and Planetary Science Letters*, *373*, 109–117. https://doi.org/10.1016/j.epsl.2013.04.027

Fichtner, A., Trampert, J., Cupillard, P., Saygin, E., Taymaz, T., Capdeville, Y., & Villaseñor, A. (2013b). Multiscale full waveform inversion. *Geophysical Journal International*, *194*(1), 534–556. https://doi.org/10.1093/gji/ggt118

Fontaine, F. R., Barruol, G., Tommasi, A., & Bokelmann, G. H. R. (2007). Upper-mantle flow beneath French Polynesia from shear wave splitting. *Geophysical Journal International*, *170*(3), 1262–1288. https://doi.org/10.1111/j.1365-246X.2007.03475.x

Fouch, M. J., & Rondenay, S. (2006). Seismic anisotropy beneath stable continental interiors. *Physics of the Earth and Planetary Interiors*, *158*(2–4), 292–320. https://doi.org/10.1016/j.pepi.2006.03.024

GEBCO Bathymetric Compilation Group 2019. (2019). *The GEBCO_2019 Grid—A continuous terrain model of the global oceans and land*. British Oceanographic Data Centre, National Oceanography Centre. https://doi.org/10.5285/836f016a-33be-6ddc-e053-6c86abc0788e

Goldstein, P., Dodge, D., Firpo, M., & Minner, L. (2003). *SAC2000: Signal processing and analysis tools for seismologists and engineers. Invited contribution to "the IASPEI International Handbook of earthquake and Engineering Seismology"*. In W. H. K. Lee, H. Kanamori, P.C. Jennings, & C. Kisslinger (Eds.). Academic Press.

Goldstein, P., & Snoke, A. (2005). SAC Availability for the IRIS Community. Incorporated Research Institutions for Seismology Newsletter.

Hatzfeld, D., Karagianni, E., Kassaras, I., Kiratzi, A., Louvari, E., Lyon-Caen, H., et al. (2001). Shear wave anisotropy in the upper mantle beneath the Aegean related to internal deformation. *Journal of Geophysical Research*, *106*(B12), 30737–30753. https://doi.org/10.1029/2001JB000387

Hayes, G. P., Moore, G. L., Portner, D. E., Hearne, M., Flamme, H., Furtney, M., & Smoczyk, G. M. (2018). Slab2, a comprehensive sub-duction zone geometry model. *Science*, *362*(6410), 58–61. https://doi.org/10.1126/science.aat4723

Herquel, G., Tapponnier, P., Wittlinger, G., Mei, J., & Danian, S. (1999). Teleseismic shear wave splitting and lithospheric beneath and across the Altyn Tagh fault. *Geophysical Research Letters*, *26*(21), 3225–3228. https://doi.org/10.1029/1999gl005387

Hollenstein, C., Kahle, H.-G., & Geiger, A. (2006). Plate tectonic framework and GPS derived strain-rate field within the boundary zones of the Eurasian and African plates. In N. Pinter, G. Gyula, J. Weber, S. Stein, & D. Medak (Eds.), *The Adria Microplate: GPS Geodesy, tectonics and Hazards*, *NATO science series: IV: Earth and environmental sciences* (Vol. 61). Springer. https://doi.org/10.1007/1-4020-4235-3_03

Holtzman, B. K., Kohlstedt, D. L., Zimmerman, M. E., Heidelbach, F., Hiraga, T., & Hus- toft, J. (2003). Melt segregation and strain partitioning: Implications for seismic anisotropy and mantle flow. *Science*, *29*(301), 1227–1230. https://doi.org/10.1126/science.1087132

Jolivet, L., & Faccenna, C. (2000). Mediterranean extension and the Africa-Eurasia collision. *Tectonics*, *19*(6), 1095–1106. https://doi.org/10.1029/2000TC900018

Jolivet, L., Faccenna, C., Becker, T., Tesauro, M., Sternai, P., & Bouilhol, P. (2018). Mantle flow and deforming continents: From India-Asia convergence to Pacific subduction. *Tectonics*, *37*(9), 2887–2914. https://doi.org/10.1029/2018TC005036

Jolivet, L., Faccenna, C., Huet, B., Labrousse, L., Le Pourhiet, L., Lacombe, L., et al. (2013). Aegean tectonics: Strain localisation, slab tearing and trench retreat. *Tectonophysics*, *597–598*, 1–33. https://doi.org/10.1016/j.tecto.2012.06.011

Jolivet, L., Faccenna, C., & Piromallo, C. (2009). From mantle to crust: Stretching the Mediterranean. *Earth and Planetary Science Letters*, *285*(1–2), 198–209. https://doi.org/10.1016/j.epsl.2009.06.017

Jung, H., & Karato, S. I. (2001). Water-induced fabric transitions in olivine. *Science*, *293*(5534), 1460–1463. https://doi.org/10.1126/science.1062235

Kaislaniemi, L., & van Hunen, J. (2014). Dynamics of lithospheric thinning and mantle melting by edge-driven convection: Application to Moroccan Atlas Mountains. *Geochemistry, Geophysics, Geosystems*, *15*(8), 3175–3189. https://doi.org/10.1002/2014GC005414

Kandilli Observatory And Earthquake Research Institute, Boğaziçi University. (1971). Bogazici University Kandilli observatory and Earthquake Research Institute [Dataset]. International Federation of Digital Seismograph Networks. https://doi.org/10.7914/SN/KO

Karabulut, H., Paul, A., Ergün, T. A., Hatzfeld, D., Childs, D. M., & Aktar, M. (2013). Long-wavelength undulations of the seismic Moho beneath the strongly stretched Western Anatolia. *Geophysical Journal International*, *194*(1), 450–464. https://doi.org/10.1093/gji/ggt100

Karato, S., Jung, H., Katayama, I., & Skemer, P. A. (2008). Geodynamic significance of seismic anisotropy of the upper mantle: New insights from laboratory studies. *Annual Review of Earth and Planetary Sciences*, *36*(1), 59–95. https://doi.org/10.1146/annurev.earth.36.031207.124120

Karato, S., & Wu, P. (1993). Rheology the upper mantle: Synthesis. *Science*, *260*(May), 771–778. https://doi.org/10.1126/science.260.5109.771

Karato, S. I. (1987). Seismic anisotropy due to lattice preferred orientation of minerals: Kinematic or dynamic? *High Pressure Research in Mineral Physics*, 455–471.

Kaviani, A., Hatzfeld, D., Paul, A., Tatar, M., & Priestley, K. (2009). Shear-wave splitting, lithospheric anisotropy, and mantle deformation beneath the Arabia–Eurasia collision zone in Iran. *Earth and Planetary Science Letters*, *286*(3–4), 371–378. https://doi.org/10.1016/j.epsl.2009.07.003

Kaviris, G., Fountoulakis, I., Spingos, I., Millas, C., Papadimitriou, P., & Drakatos, G. (2018). Mantle dynamics beneath Greece from SKS and PKS seismic anisotropy study. *Acta Geophysica*, *66*(6), 1341–1357. https://doi.org/10.1007/s11600-018-0225-z

Kennett, B., & Engdahl, E. (1991). Traveltimes for global earthquake location and phase identification. *Geophysical Journal International*, *105*(2), 429–465. https://doi.org/10.1111/j.1365-246x.1991.tb06724.x

Kennett, B. L. N., Engdahl, E. R., & Buland, R. (1995). Constraints on seismic velocities in the Earth from traveltimes. *Geophysical Journal International*, *122*(1), 108–124. https://doi.org/10.1111/j.1365-246X.1995.tb03540.x

Kind, R., Eken, T., Tilmann, F., Sodoudi, F., Taymaz, T., Bulut, F., et al. (2015). Thickness of the lithosphere beneath Turkey and surroundings from S-receiver functions. *Solid Earth*, *6*(3), 971–984. https://doi.org/10.5194/se-6-971-2015

King, S. D., & Anderson, D. L. (1998). Edge-driven convection. *Earth and Planetary Science Letters*, *160*(3–4), 289–296. https://doi.org/10.1016/s0012-821x(98)00089-2

Kissel, C., & Laj, C. (1988). The tertiary geodynamical evolution of the Aegean arc: A paleomagnetic reconstruction. *Tectonophysics*, *146*(1–4), 183–201. https://doi.org/10.1016/0040-1951(88)90090-x

Kohlstedt, D. L., & Holtzman, B. K. (2009). Shearing melt out of the Earth: An experimentalist's perspective on the influence of deformation on melt extraction. *Annual Review of Earth and Planetary Sciences*, *37*(1), 561–593. https://doi.org/10.1146/annurev.earth.031208.100104

Kömeç-Mutlu, A., & Karabulut, H. (2011). Anisotropic Pn tomography of Turkey and adjacent regions. *Geophysical Journal International*, *187*(3), 1743–1758. https://doi.org/10.1111/j.1365-246X.2011.05235.x

Kounoudis, R., Bastow, I. D., Ogden, C. S., Goes, S., Jenkins, J., Grant, B., & Braham, C. (2020). Seismic tomographic imaging of the eastern Mediterranean mantle: Implications for terminal-stage subduction, the uplift of Anatolia, and the development of the North Anatolian Fault. *Geochemistry, Geophysics, Geosystems*, *21*(7). https://doi.org/10.1029/2020GC009009

Kreemer, C., Chamot-Rooke, N., & Le Pichon, X. (2004). Constraints on the evolution and vertical coherency of deformation in the Northern Aegean from a comparison of geodetic, geologic and seismologic data. *Earth and Planetary Science Letters*, *225*(3–4), 329–346. https://doi.org/10.1016/j.epsl.2004.06.018

Kufner, S. K., Eken, T., Tilmann, F., Schurr, B., Yuan, X., Mechie, J., et al. (2018). Seismic anisotropy beneath the Pamir and the Hindu Kush: Evidence for contributions from crust, mantle lithosphere, and asthenosphere. *Journal of Geophysical Research: Solid Earth*, *123*(12), 10727–10748. https://doi.org/10.1029/2018JB015926

Lemnifi, A. A., Elshaafi, A., Karaoğlu, Ö., Salah, M. K., Aouad, N., Reed, C. A., & Yu, Y. (2017). Complex seismic anisotropy and mantle dynamics beneath Turkey. *Journal of Geodynamics*, *112*, 31–45. https://doi.org/10.1016/j.jog.2017.10.004

León Soto, G., Sandvol, E., Ni, J. F., Flesch, L., Hearn, T. M., Tilmann, F., et al. (2012). Significant and vertically coherent seismic anisotropy beneath eastern Tibet. *Journal of Geophysical Research*, *117*(B5). https://doi.org/10.1029/2011JB008919

Le Pichon, X., & Angelier, J. (1979). The Hellenic arc and trench system: A key to the neotectonic evolution of the eastern Mediterranean area. *Tectonophysics*, *60*(1–2), 1–42. https://doi.org/10.1016/0040-1951(79)90131-8

Le Pichon, X., & Kreemer, C. (2010). The Miocene-to-present kinematic evolution of the eastern Mediterranean and Middle East and its implications for dynamics. *Annual Review of Earth and Planetary Sciences*, *38*(1), 323–351. https://doi.org/10.1146/annurev-earth-040809-152419

Licciardi, A., Eken, T., Taymaz, T., Piana Agostinetti, N., & Yolsal-Çevikbilen, S. (2018). Seismic anisotropy in central North Anatolian Fault Zone and its implications on crustal deformation. *Physics of the Earth and Planetary Interiors*, *277*, 99–112. https://doi.org/10.1016/j.pepi.2018.01.012

Mascle, J., & Martin, L. (1990). Shallow structure and recent evolution of the Aegean Sea: A synthesis based on continuous reflection profiles. *Marine Geology*, *94*(4), 271–299. https://doi.org/10.1016/0025-3227(90)90060-W

McClusky, S., Balassanian, S., Barka, A., Demir, C., Ergintav, S., Georgiev, I., et al. (2000). Global Positioning System constraints on plate kinematics and dynamics in the eastern Mediterranean and Caucasus. *Journal of Geophysical Research*, *105*(B3), 5695–5719. https://doi.org/10.1029/1999jb900351

McClusky, S., Reilinger, R., Mahmoud, S., Ben Sari, D., & Tealeb, A. (2003). GPS constraints on Africa (Nubia) and Arabia plate motions. *Geophysical Journal International*, *155*(1), 126–138. https://doi.org/10.1046/j.1365-246x.2003.02023.x

McKenzie, D. (1972). Active tectonics of the Mediterranean region. *Geophysical Journal International*, *30*(2), 109–185. https://doi.org/10.1111/j.1365-246x.1972.tb02351.x

McKenzie, D. (1978). Some remarks on the development of sedimentary basins. *Earth and Planetary Science Letters*, *40*(1), 25–32. https://doi.org/10.1016/0012-821x(78)90071-7

McKenzie, D. (2020). The structure of the lithosphere and upper mantle beneath the Eastern Mediterranean and Middle East. *Mediterranean Geoscience Reviews*, *2*(3), 311–326. https://doi.org/10.1007/s42990-020-00038-1

Meijer, P. T., & Wortel, M. (1997). Present-day dynamics of the Aegean region: A model analysis of the horizontal pattern of stress and deformation. *Tectonics*, *16*(6), 879–895. https://doi.org/10.1029/97tc02004

Merry, T. A. J., Bastow, I. D., Kounoudis, R., Ogden, C. S., Bell, R. E., & Jones, L. (2021). The influence of the North Anatolian Fault and a fragmenting slab architecture on upper mantle seismic anisotropy in the eastern Mediterranean. *Geochemistry, Geophysics, Geosystems*, *22*(9), 1–36. https://doi.org/10.1029/2021GC009896

National Observatory of Athens, Institute of Geodynamics, Athens. (1975). National observatory of Athens seismic network [Dataset]. International Federation of Digital Seismograph Networks. https://doi.org/10.7914/SN/HL

Niu, F., & Li, J. (2011). Component azimuths of the CEArray stations estimated from P-wave particle motion. *Earthquake Science*, *24*(1), 3–13. https://doi.org/10.1007/s11589-011-0764-8

Nocquet, J.-M. (2012). Present-day kinematics of the Mediterranean: A comprehensive overview of GPS results. *Tectonophysics*, *579*, 220–242. https://doi.org/10.1016/j.tecto.2012.03.037

Okay, A. I. (2008). Geology of Turkey: A synopsis. *Der Anschnitt*, *21*, 19–42.

Okay, A. I., & Tüysüz, O. (1999). Tethyan sutures of northern Turkey. *Geological Society, London, Special Publications*, *156*(1), 475–515. https://doi.org/10.1144/gsl.sp.1999.156.01.22

Olive, J. A., Pearce, F., Rondenay, S., & Behn, M. D. (2014). Pronounced zonation of seismic anisotropy in the Western Hellenic subduction zone and its geodynamic significance. *Earth and Planetary Science Letters*, *391*, 100–109. https://doi.org/10.1016/j.epsl.2014.01.029

Özeren, M. S. (2012). Crust-mantle mechanical coupling in eastern Mediterranean and eastern Turkey. *Proceedings of the National Academy of Sciences*, *109*(22), 8429–8433. https://doi.org/10.1073/pnas.1201826109

Özeren, M. S., & Holt, W. E. (2010). The dynamics of the eastern Mediterranean and eastern Turkey. *Geophysical Journal International*, *183*(3), 1165–1184. https://doi.org/10.1111/j.1365-246X.2010.04819.x

Paul, A., Karabulut, H., Kömeç-Mutlu, A., & Salaün, G. (2014). A comprehensive and densely sampled map of shear-wave azimuthal anisotropy in the Aegean–Anatolia region. *Earth and Planetary Science Letters*, *389*, 14–22. https://doi.org/10.1016/j.epsl.2013.12.019

Piromallo, C., & Morelli, A. (2003). P wave tomography of the mantle under the Alpine-Mediterranean area. *Journal of Geophysical Research*, *108*(B2), 2065. https://doi.org/10.1029/2002jb001757

Polet, J., & Kanamori, H. (2002). Anisotropy beneath California: Shear wave splitting measurements using a dense broadband array. *Geophysical Journal International*, *149*(2), 313–327. https://doi.org/10.1046/j.1365-246X.2002.01630.x

Portner, D. E., Delph, J. R., Berk Biryol, C., Beck, S. L., Zandt, G., Özacar, A. A., et al. (2018). Subduction termination through progressive slab deformation across Eastern Mediterranean subduction zones from updated P-wave tomography beneath Anatolia. *Geosphere*, *14*(3), 907–925. https://doi.org/10.1130/GES01617.1

Reilinger, R., McClusky, S., Vernant, P., Lawrence, S., Ergintav, S., Cakmak, R., et al. (2006). GPS constraints on continental deformation in the Africa-Arabia-Eurasia continental collision zone and implications for the dynamics of plate interactions. *Journal of Geophysical Research*, *111*(5), 1–26. https://doi.org/10.1029/2005jb004051

Revenaugh, J., & Reasoner, C. (1997). Cumulative offset of the San Andreas Fault in central California: A seismic approach. *Geology*, *25*(2), 123–126. https://doi.org/10.1130/0091-7613(1997)025<0123:COOTSA>2.3.CO;2

Rümpker, G., Ryberg, T., Bock, G., & Desert Seismology Group (2003). Boundary-layer mantle flow under the Dead Sea transform fault inferred from seismic anisotropy. *Nature*, *425*(6957), 497–501. https://doi.org/10.1038/nature01982

Salaün, G., Pedersen, H. A., Paul, A., Farra, V., Karabulut, H., Hatzfeld, D., et al. (2012). High-resolution surface wave tomography beneath the Aegean-Anatolia region: Constraints on upper-mantle structure. *Geophysical Journal International*, *190*(1), 406–420. https://doi.org/10.1111/j.1365-246x.2012.05483.x

Saltogianni, V., Gianniou, M., Taymaz, T., Yolsal-Çevikbilen, S., & Stiros, S. (2015). Fault slip source models for the 2014 Mw 6.9 Samothraki-Gökçeada earthquake (North Aegean Trough) combining geodetic and seismological observations. *Journal of Geophysical Research: Solid Earth*, *120*(12), 8610–8622. https://doi.org/10.1002/2015jb012052

Sandvol, E., Turkelli, N., Zor, E., Gok, R., Bekler, T., Gurbuz, C., et al. (2003). Shear wave splitting in a young continent-continent collision: An example from Eastern Turkey. *Geophysical Research Letters*, *30*(24), 2–5. https://doi.org/10.1029/2003GL017390

Şaroğlu, F., Emre, Ö., & Kuşçu, I. (1992). *Active Fault map of Turkey (3 sheets, 1:100.000 scale)*. General Directorate of Mineral Research and Exploration, MTA.

Saunders, P., Priestley, K., & Taymaz, T. (1998). Variations in the crustal structure beneath Western Turkey. *Geophysical Journal International*, *134*(2), 373–389. https://doi.org/10.1046/j.1365-246x.1998.00571.x

Savage, M. K. (1999). Seismic anisotropy and mantle deformation: What have we learned from shear wave splitting? *Reviews of Geophysics*, *37*(1), 65–106. https://doi.org/10.1029/98RG02075

Schmid, C., van der Lee, S., & Giardini, D. (2004). Delay times and shear wave splitting in the Mediterranean region. *Geophysical Journal International*, *159*(1), 275–290. https://doi.org/10.1111/j.1365-246x.2004.02381.x

Şengör, A. M., Tüysüz, O., İmren, C., Sakınç, M., Eyidoğan, H., Görür, N., et al. (2005). The North Anatolian Fault: A new look. *Annual Review of Earth and Planetary Sciences*, *33*(1), 37–112. https://doi.org/10.1146/annurev.earth.32.101802.120415

Şengör, A. M. C., Görür, N., & Şaroğlu, F. (1985). Strike-slip faulting and related basin formation in zones of tectonic escape: Turkey as a case study. In K. T. Biddle & N. Christie- Blick (Eds.), *Strike-slip deformation, basin formation and Sedimentation* (Vol. 37, pp. 227–264). Society of Economic Mineralogist and Paleontologists Special Publication.

Silver, P. G., & Chan, W. W. (1991). Shear wave splitting and subcontinental mantle deformation. *Journal of Geophysical Research*, *96*(B10), 16429. https://doi.org/10.1029/91jb00899

Silver, P. G., & Savage, M. K. (1994). The interpretation of shear-wave splitting parameters in the presence of two anisotropic layers. *Geophysical Journal International*, *119*(3), 949–963. https://doi.org/10.1111/j.1365-246X.1994.tb04027.x

Sodoudi, F., Kind, R., Hatzfeld, D., Priestley, K., Hanka, W., Wylegalla, K., et al. (2006). Lithospheric structure of the Aegean obtained from P and S receiver functions. *Journal of Geophysical Research*, *111*(B12). https://doi.org/10.1029/2005jb003932

Taymaz, T. (1996). S-P-wave traveltime residuals from earthquakes and lateral inhomogeneity in the upper mantle beneath the Aegean and the Hellenic Trench near Crete. *Geophysical Journal International*, *127*(2), 545–558. https://doi.org/10.1111/j.1365-246x.1996.tb04740.x

Taymaz, T., Jackson, J., & Mckenzie, D. (1991). Active tectonics of the north and central Aegean Sea. *Active Tectonics of the North and Central Aegean Sea*, *106*(2), 433–490. https://doi.org/10.1111/j.1365-246x.1991.tb03906.x

Taymaz, T., Jackson, J., & Westaway, R. (1990). Earthquake mechanisms in the Hellenic Trench near Crete. *Geophysical Journal International*, *102*(3), 695–731. https://doi.org/10.1111/j.1365-246x.1990.tb04590.x

Taymaz, T., Westaway, R., & Reilinger, R. (Eds.) (2004). Active faulting and crustal deformation in the eastern Mediterranean region. Tectonophysics (Vol. *391*, pp. 1–374).

Taymaz, T., Yilmaz, Y., & Dilek, Y. (2007). The geodynamics of the Aegean and Anatolia: Introduction. *Geological Society, London, Special Publications*, *291*(1), 1–16. https://doi.org/10.1144/SP291.1

Taymaz, T., Yolsal-Çevikbilen, S., Irmak, T. S., Vera, F., Liu, C., Eken, T., et al. (2022). Kinematics of 30 October 2020 Mw 7.0 Neon Karlovasion (Samos) earthquake in the eastern Aegean Sea: Implications on source characteristics and dynamic rupture simulations. *Tectonophysics*, *826*, 229223. https://doi.org/10.1016/j.tecto.2022.229223

Teanby, N. A., Kendall, J. M., & van der Baan, M. (2004). Automation of shear-wave splitting measurements using cluster analysis. *Bulletin of the Seismological Society of America*, *94*(2), 453–463. https://doi.org/10.1785/0120030123

Tirel, C., Gueydan, F., Tiberi, C., & Brun, J. P. (2004). Aegean crustal thickness inferred from gravity inversion. Geodynamical implications. *Earth and Planetary Science Letters*, *228*(3–4), 267–280. https://doi.org/10.1016/j.epsl.2004.10.023

Tozer, B., Sandwell, D. T., Smith, W. H. F., Olson, C., Beale, J. R., & Wessel, P. (2019). Global bathymetry and topography at 15 arc sec: SRTM15+. *Earth and Space Science*, *6*(10), 1847–1864. https://doi.org/10.1029/2019EA00065

Vanacore, E. A., Taymaz, T., & Saygin, E. (2013). Moho structure of the anatolian plate from receiver function analysis. *Geophysical Journal International*, *193*(1), 329–337. https://doi.org/10.1093/gji/ggs107

Vecsey, L., Plomerová, J., & Babuška, V. (2008). Shear-wave splitting measurements—Problems and solutions. *Tectonophysics*, *462*(1–4), 178–196. https://doi.org/10.1016/j.tecto.2008.01.021

Vinnik, L., Oreshin, S., & Erduran, M. (2016). Melt in the mantle and seismic azimuthal anisotropy: Evidence from Anatolia. *Geophysical Journal International*, *205*(1), 523–530. https://doi.org/10.1093/gji/ggw021

Vinnik, L. P., Makeyeva, L. I., Milev, A., & Usenko, A. Y. (1992). Global patterns of azimuthal anisotropy and deformations in the continental mantle. *Geophysical Journal International*, *111*(3), 433–447. https://doi.org/10.1111/j.1365-246x.1992.tb02102.x

Walker, K. T., Bokelmann, G. H. R., Klemperer, S. L., & Bock, G. (2005). Shear-wave splitting around the Eifel hotspot: Evidence for a mantle upwelling. *Geophysical Journal International*, *163*(3), 962–980. https://doi.org/10.1111/j.1365-246x.2005.02636.x

Wang, H., Huang, Z., Eken, T., Keleş, D., Kaya-Eken, T., Confal, J. M., et al. (2020). Isotropic and anisotropic P wave velocity structures of the crust and uppermost mantle beneath Turkey. *Journal of Geophysical Research: Solid Earth*, *125*(12). https://doi.org/10.1029/2020JB019566

Wei, W., Zhao, D., Wei, F., Bai, X., & Xu, J. (2019). Mantle dynamics of the eastern Mediterranean and Middle East: Constraints from P-wave anisotropic tomography. *Geochemistry, Geophysics, Geosystems*, *20*(10), 4505–4530. https://doi.org/10.1029/2019GC008512

Wessel, P., & Smith, W. (1998). New, improved version of generic mapping tools released. *Eos, Transactions American Geophysical Union*, *79*(47), 579. https://doi.org/10.1029/98eo00426

Wolfe, C. J., & Silver, P. G. (1998). Seismic anisotropy of oceanic upper mantle: Shear wave splitting methodologies and observations. *Journal of Geophysical Research*, *103*(B1), 749–771. https://doi.org/10.1029/97jb02023

Yolsal-Çevikbilen, S. (2014). Seismic anisotropy along the Cyprean arc and northeast Mediterranean Sea inferred from shear wave splitting analysis. *Physics of the Earth and Planetary Interiors*, *233*, 112–134. https://doi.org/10.1016/j.pepi.2014.05.010

Yolsal-Çevikbilen, S., Biryol, C. B., Beck, S., Zandt, G., Taymaz, T., Adiyaman, H. E., & Özacar, A. A. (2012). 3-D crustal structure along the North Anatolian Fault Zone in north-central Anatolia revealed by local earthquake tomography. *Geophysical Journal International*, *188*, 819–849. https://doi.org/10.1111/j.1365-246X.2011.05313.x

Yolsal-Çevikbilen, S., & Taymaz, T. (2012). Earthquake source parameters along the Hellenic subduction zone and numerical simulations of historical tsunamis in the Eastern Mediterranean. *Tectonophysics*, *536–537*, 61–100. https://doi.org/10.1016/j.tecto.2012.02.019

Yolsal-Çevikbilen, S., Taymaz, T., & Helvacı, C. (2014). Earthquake mechanisms in the Gulfs of Gökova, Sığacık, Kuşadası, and the Simav region (Western Turkey): Neotectonics, seismotectonics and geodynamic implications. *Techtonophysics*, *635*, 100–124. https://doi.org/10.1016/j.tecto.2014.05.001

Zhang, S., & Karato, S. I. (1995). Lattice preferred orientation of olivine aggregates deformed in simple shear. *Nature*, *375*(6534), 774–777. https://doi.org/10.1038/375774a0

References From the Supporting Information

Bianchi, I., Park, J., Piana Agostinetti, N., & Levin, V. (2010). Mapping seismic anisotropy using harmonic decomposition of receiver functions: An application to Northern Apennines, Italy. *Journal of Geophysical Research*, *115*(B12), B12317. https://doi.org/10.1029/2009JB007061

Di Bona, M. (1998). Variance estimate in frequency-domain deconvolution for teleseismic receiver function computation. *Geophysical Journal International*, *134*(2), 634–646. https://doi.org/10.1111/j.1365-246X.1998.00523.x